Toward quantitative wall shear stress measurements: a comparative study on the impact of *RGB*-to-hue conversion algorithms on liquid crystal diagnostics

OPEN ACCESS
IOP Publishing
Measurement Science and Technology
Meas. Sci. Technol. **34** (2023) 015203 (21pp)
https://doi.org/10.1088/1361-6501/ac8f63

Toward quantitative wall shear stress measurements: a comparative study on the impact of *RGB*-to-hue conversion algorithms on liquid crystal diagnostics

Stefanos Melekidis*, Maximilian Rolf Elfner[1] and Hans-Jörg Bauer

Institute of Thermal Turbomachinery (ITS), Karlsruhe Institute of Technology (KIT), Kaiserstrasse 12, Karlsruhe, Germany

E-mail: stefanos.melekidis@kit.edu

Received 9 March 2022, revised 9 August 2022
Accepted for publication 5 September 2022
Published 21 October 2022

Abstract

Liquid crystal diagnostics is a capable tool for determining quantitative wall shear stress distributions with high spatial resolution, which can be applied to almost any surface shape. A standard consumer camera is typically used to record the scattered light of the liquid crystals as red, green, and blue *RGB* data. This *RGB* data has to be converted to a hue-based color space in order to perform a state-of-the-art calibration procedure. Algorithms for this purpose are numerous in the literature. However, a considerable number of them show a wide range of resulting hue values due to different trigonometric relations. This renders some conversion algorithms unsuitable for calculating physical wall shear stresses, as their magnitude and distribution depend on the conversion algorithm used. For this reason, the choice of an inappropriate conversion algorithm may compromise the measurement accuracy and subsequent comparability significantly. The main objective of this paper is to give recommendations for the use of appropriate algorithms to determine physical wall shear stresses. In a first step, synthetic liquid crystal data is converted using algorithms described in the literature. The preselected algorithms are then applied to liquid crystal data from a flat plate wind tunnel experiment to illustrate their influence on the determined uncalibrated wall shear stress distribution. The final discussion serves as guidelines for the post-processing of liquid crystal data and their subsequent comparability.

Keywords: liquid crystals, wall shear stress, hue conversion, image processing, commercial consumer camera, experimental data, calibration

(Some figures may appear in colour only in the online journal)

[1] Is no longer at Karlsruhe Institute of Technology.
* Author to whom any correspondence should be addressed.

Nomenclature

Latin

H	°	Hue
H_τ	°	Relative wall shear stress or vector-aligned hue (H at ϕ_τ)
I_{gray}	A.U.	Intensity, e.g. pixel-based gray-scale
L_{char}	m	Characteristic length
$\{R, G, B\}$	A.U.	Red, green, and blue detector signal in s*RGB* color space
S	A.U.	Saturation
X	A.U.	Brightness, intensity, lightness, or value
c	A.U.	Arbitrary constant
c_{f}	—	Skin friction coefficient
j	—	Exponent
m	—	Arbitrary constant (slope)
m	—	Number of circumferential positions
n	—	Number of images for averaging
n	—	Refractive index
p	m	Pitch of helix structure
s	—	Amplification factor
t	s	Integration time
u	m s^{-1}	Streamwise velocity
x	m	Streamwise coordinate
y	m	Wall-normal coordinate
z	m	Lateral coordinate

Greek

α_{c}	°	Above-plane viewing angle (polar)
θ	—	Intermediate angle (only for calculation)
ϑ_{i}	°	Illumination angle
ϑ_{o}	°	Observation angle
κ	—	Karman constant
λ	m	Dominant wavelength
μ	Pa s	Dynamic viscosity
ρ	kg m^{-3}	Density
σ	A.U.	Standard deviation
σ_{rel}	%	Variation coefficient
τ	Pa	Wall shear stress magnitude
ϕ_τ	°	Angle at vector-aligned hue (ϕ at H_τ)
ϕ_{c}	°	Circumferential viewing angle (azimuthal)

Scripts

$\bar{\square}$	Averaged value
$\square_{\text{col}}$	Collimated light
$\square_{\text{dif}}$	Diffuse light
$\square_{\text{eo}}$	Extraordinary
$\square_{\text{ideal}}$	Ideal
$\square_{\text{lc}}$	Liquid crystals
$\square_{\text{max}}$	Maximum
$\square_{\text{min}}$	Minimum
$\square_{\text{o}}$	Ordinary

Similarity parameters

$\text{Re} = \frac{u \rho L_{\text{char}}}{\mu}$	Reynolds number
$\text{Tu} = C \left(\frac{x}{d}\right)^{-5/7}$	Free-stream turbulence intensity according to Roach [1]

Abbreviations

JPEG	Joint Photographic Experts Group
pdf	Probability density function
sRGB	Standard *RGB* (red, green, blue) color space

1. Toward quantitative wall shear stress measurements using liquid crystal diagnostics

Information on the wall shear stress magnitude, and its direction is essential to improve the aerodynamic design of components. Conventional techniques such as mechanical float balances, Preston tubes, hot-wire anemometry, or hot-film measuring devices are used to determine wall shear stresses. All of these may provide accurate and partly high-frequency data. However, such sensors only cover the area-averaged target value of the measured variable or provide local information at specific points on a surface. Furthermore, their intrusive use may influence the flow considerably. More importantly, the spatial dimensions of conventional sensors limit the spatial resolution of the measurement technique. Consequently, determining detailed two-dimensional field information about the wall shear stress on an arbitrarily shaped surface requires the use of numerous sensors, each of which has to be attached to the surface under investigation. This, however, is often not possible, can be time-consuming and costly, and disturbs the boundary layer even more. On top of that, such sensors influence each other when they are mounted too close to each other. This results in the demand for a quantitative, non-intrusive, robust, and easy-to-use measurement technique with high spatial resolution. In this context, the liquid crystal measurement technique can make full use of its advantages. In particular, of being non-intrusive and of having a high spatial resolution, with which data can be provided. The research conducted by Reda and Muratore [2] yields that liquid crystal diagnostics in combination with so-called Fringe-Imaging Skin Friction, or simply oil drop interferometry, can fulfill these requirements. Therefore, liquid crystal diagnostics may be used in many technical applications to provide information on locally resolved wall shear stress vector fields with high resolution and, if correctly calibrated, with low error. Thus, liquid crystal diagnostics is further researched [2–4]. However, it is evident that the acquisition and evaluation of the recorded color signal are prone to errors. To elaborate further, the fundamentals of light propagation and scattering in liquid crystals are described.

Liquid crystals[2] selectively scatter incident light of the visible spectrum. This is due to the characteristic length of the liquid crystals, the pitch p[3], which is in the order of magnitude of the wavelength λ of visible light and the following properties:

[2] In the following, the optically active chiral-nematic phase is referred to exclusively. More information on the classification of liquid crystals and their mesophases is given in appendix A, see figure A1.

[3] The pitch defines the distance between two molecular planes between which the director has rotated 360°, ergo has the same preferred orientation, see appendix A, figure A1.

- **Birefringence:** Optical birefringence results from the anisotropy of the liquid crystal molecules. Incident unpolarized light is subjected to different refractive indices depending on the direction of propagation. A distinction is made between an ordinary refractive index n_o and an extraordinary one n_eo. The two resulting linearly polarized partial rays leaving the molecule are polarized orthogonally to each other. The difference of the refractive indices $\Delta n = n_\mathrm{o} - n_\mathrm{eo}$ serves as a measure of the birefringence [5].
- **Circular dicroism:** Linear polarization of light results from crystal-structural optical phenomena. It can be represented by two oppositely circularly polarized waves. These are described as left-handed circularly polarized and right-handed circularly polarized, respectively [6]. At $\lambda \approx p$, strong scattering of circularly polarized light occurs, provided it has the same direction of rotation as the chiral-nematic structure. The light rotating in the opposite direction is almost completely transmitted through the liquid crystal structure.

According to Stegemeyer [6], the reflection maximum, which corresponds to the dominant wavelength of the scattered light can be calculated using

$$\lambda = \bar{n}p, \tag{1}$$

even though the calculation of the maximum wavelength of the scattered light is valid only to light incident perpendicularly to the liquid crystal layer [5]. The mean refractive index $\bar{n}$ is calculated by $\frac{1}{2}(n_\mathrm{o} + n_\mathrm{eo})$. Thus, the wavelength at the reflection maximum depends on the average of the refractive indices of the ordinary and extraordinary rays and the pitch of the helix. Due to the anisotropy of the liquid crystal molecules, incident light is refracted with different refractive indices within the refractive index interval Δn, such that not only light of a single wavelength but the light of different wavelengths is reflected. The scattering occurs symmetrically around the maximum wavelength of the scattered light in a wavelength range of $\Delta\lambda = \Delta np$ and is therefore referred to as selective scattering of light. With varying pitch of the helical structure, the selective scattering of light changes according to equation (1). This change in wavelength is used for determining wall shear stresses by means of liquid crystal diagnostics. Due to the layered arrangement of the liquid crystals, refraction effects superimpose and the selectively scattered waves interfere. Using Bragg's theory, equation (1) can be extended to

$$\lambda = \bar{n}p\cos(\vartheta_\mathrm{i}). \tag{2}$$

Thus, the dominant wavelength of the selectively scattered light can be determined even for non-orthogonal incidence of light ϑ_i relative to the liquid crystal surface. By further extending equation (2), the wavelength of the scattered light can be described as a function of the illumination angle ϑ_i and observation angle ϑ_o, as in Fergason [7]

$$\lambda = \bar{n}p\cos\left\{\frac{1}{2}\left(\sin^{-1}\left(\frac{\sin(\vartheta_\mathrm{i})}{\bar{n}}\right) + \sin^{-1}\left(\frac{\sin(\vartheta_\mathrm{o})}{\bar{n}}\right)\right)\right\}. \tag{3}$$

Based on the introduced equations describing incident light and the selective scattering, a substitute quantity, the hue, can be identified, which is alternatively used in the literature instead of the wavelength [8]. Reda and Muratore [2] and Reda *et al* [8] carry out liquid crystal measurements both using spectroscopy (spectrometer, wavelength, point data) and photogrammetry (camera, *RGB* and hue, respectively, two-dimensional data) and show that wall shear stress vector fields can be determined using both quantities. Based on their findings, they formulate a hue-based approach [2] which is also used in this paper to determine wall shear stress vector fields from liquid crystal colors.

Typically, this data is acquired with a standard consumer camera. The selectively scattered light rays of different wavelengths incide on an image sensor and are available as intensity values after additional amplification and analog/digital conversion. After further processing of the intensity values (debayering/demosaicing), these may be in the form of red, green, and blue values (*RGB*) and are available in the standard *RGB* (s*RGB*) color space, using the *RGB* color model.

Like the pixel-based intensity, e.g. gray-scale values I_gray, the debayered *RGB* values are significantly dependent on the intensity of the selectively scattered light, which in turn is predetermined by the illumination source used. Based on the relation between intensity and *RGB* values, the captured liquid crystal signal is found to be illumination-variant. However, the pitch and thus the wavelength (frequency) of the light is relevant to the selective scattering and not the intensity (amplitude), see equations (1)–(3).

This physical fact motivates a decorrelation of the intensity of the color values. This can be achieved by modal/dimensionality reduction methods such as Proper Orthogonal Decomposition [9] or by converting the *RGB* data into the *HSX* color system using an appropriate conversion algorithm, where H is the hue, the equivalent to the dominant wavelength, hence $\lambda \propto mH^{-1}$, with m being a constant affecting the slope, S the saturation, and X[4] the intensity.

To determine wall shear stresses, liquid crystal mixtures are used whose helix pitch depends mainly on the wall shear stress τ and only to a negligible extent on temperature and pressure. This results in the relation

$$p \propto \lambda \propto \tau^{-\mathrm{j}} \quad \text{with } j > 0, \tag{4}$$

between pitch, wavelength of the scattered light, and wall shear stress, with j being an exponent larger than zero. Consequently, an increase in the wall shear stress is related to a shorter wavelength of the selectively scattered light, resulting from a decrease in the helical pitch.

[4] X constitutes the third quantity of the color systems and represents brightness/intensity/lightness/value [10]. In section 3, a distinction is made because the individual quantities are partly calculated differently.

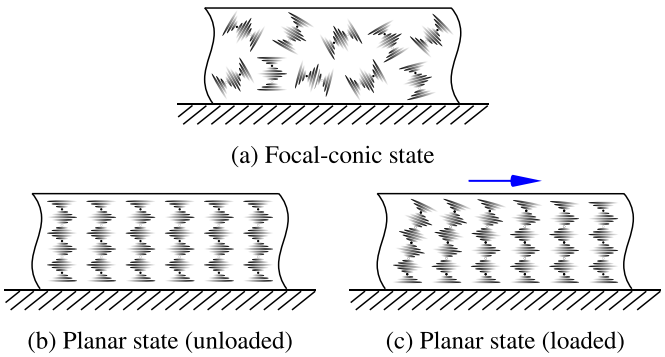

Figure 1. Structures of chiral-nematic liquid crystal coatings for wall shear stress measurements: molecules before (a) and after alignment (b) as well as during load (c) according to Bonnett [11]. The flow direction is illustrated by the blue arrow.

To use the derived dependencies and the given relation in equation (4), an ordered alignment of the optical axis of the helical structure is required. The texture transition from a disordered to an ordered structure can be achieved by prior alignment of the molecules. This can be done, for example, by shearing the liquid crystal coating using a stream of compressed air over the coating or by fine brushing. The three states relevant to measuring wall shear stresses are illustrated in figure 1.

In the focal-conic state, see figure 1(a), the axes of the helices are disordered and at a low energy level. This texture is birefringent but optically semi-active, such that incident light in the classical physical sense is only scattered randomly and not selectively. The optically active planar or Grandjean texture of the liquid crystal layer, see figure 1(b), has a specific perceptible color. The helical axes are ordered and orthogonally to the coated surface. However, there is no selective scattering of light at this point. From figure 1(c), it appears that in addition to the change in the pitch of the helix due to temperature changes, there is a tilting of the helical axes due to the flow-induced shear forces along the surface. This means that the scattering of light due to the change in pitch of the chiral-nematic liquid crystal planes is complemented by the selective scattering of light due to the tilting of the helical axes under load. This is the key feature why wall shear stresses can be visualized using liquid crystals and subsequently quantified using a suitable calibration.

In summary, the resulting selectively scattered light is captured and then converted utilizing a conversion algorithm. These conversion algorithms are numerous in the literature. Some of them have significant differences in the magnitudes of the resulting hues. Due to the proportionality between hue and wall shear stress, see equation (4), and the resulting different wall shear stress fields and magnitudes for the same (*in-situ*) calibration and database, but using different conversion algorithms, they are investigated for their suitability to determine physical wall shear stress distributions. For this purpose, requirements are defined that have to be satisfied by the conversion algorithms. The quantitative evaluation of the converted values is based on the assumption that wavelength and hue are linearly related in a range relevant to liquid crystal diagnostics. This assumption is confirmed by Wilder and Reda [12]. The evaluated algorithms are then applied to experimental liquid crystal data from a flat plate wind tunnel to illustrate their impact on the measured wall shear stress distribution, specifically the magnitude and its direction.

2. Liquid crystal diagnostics: data acquisition and hue-based approach

Based on the described selective scattering of light as a function of the local wall shear stress and the geometric coherences, a three-dimensional color spectrum results, see figure 2. This can be visualized depending on the illumination angle chosen orthogonally to the region of interest and the introduced observation angle, see equation (3), relative to the aligned liquid crystal layer, see figure 1(c).

Reda and Muratore [2] generalize the observation angle from Fergason's two-dimensional consideration, see equation (3), by one additional dimension, introducing an azimuth angle ϕ_c, referred to as circumferential viewing angle, and a polar angle α_c, referred to as above-plane viewing angle. The circumferential viewing angle is used to describe the position of an observer in the xz-plane of the liquid crystal surface. The above-plane viewing angle indicates the inclination of an observer relative to this plane. Reda and Muratore's results allow the conclusion that the minimum dominant wavelength can be measured if the direction of the wall shear stress vector corresponds to the observation direction and points away from the observer, e.g. the blue color in direction of the flow. At fixed circumferential viewing angle, the strength of the color signal depends on the above-plane viewing angle. The larger the latter, the longer the wavelength of the selectively scattered light, e.g. the color characteristic from blue (λ_{min}) to red (λ_{max}). This azimuthal and polar angle-dependent selective scattering of light occurs only when the liquid crystals are stressed, e.g. by an air flow along a flat plate which is indicated by a turbulent velocity profile with the flow directions pointing in the x-direction, represented by the blue arrows, see figure 2.

Based on these findings, Reda and Muratore propose a calibration method to quantify wall shear stresses, in both magnitude and direction, which is described in figure 3. Using this method, a wall shear stress vector field can be determined, recording the selectively scattered light, which results from the wall shear stress-induced change in the pitch of the liquid crystals, see section 1. By calibrating the acquired values in the wall shear stress direction in relation to the prevailing local wall shear stress magnitude, the vector field may be calculated according to steps **I** to **IV**. In the following, it is assumed that both the illumination and camera settings and the above-plane viewing angle remain unchanged throughout the entire experiment. A suitable experimental setup, with well-defined boundary conditions for the calibration of the liquid crystal signal, is presented by Melekidis *et al* [14].

In step **I**, see figure 3, the color response of a liquid crystal sample at a known magnitude and direction of wall shear stress

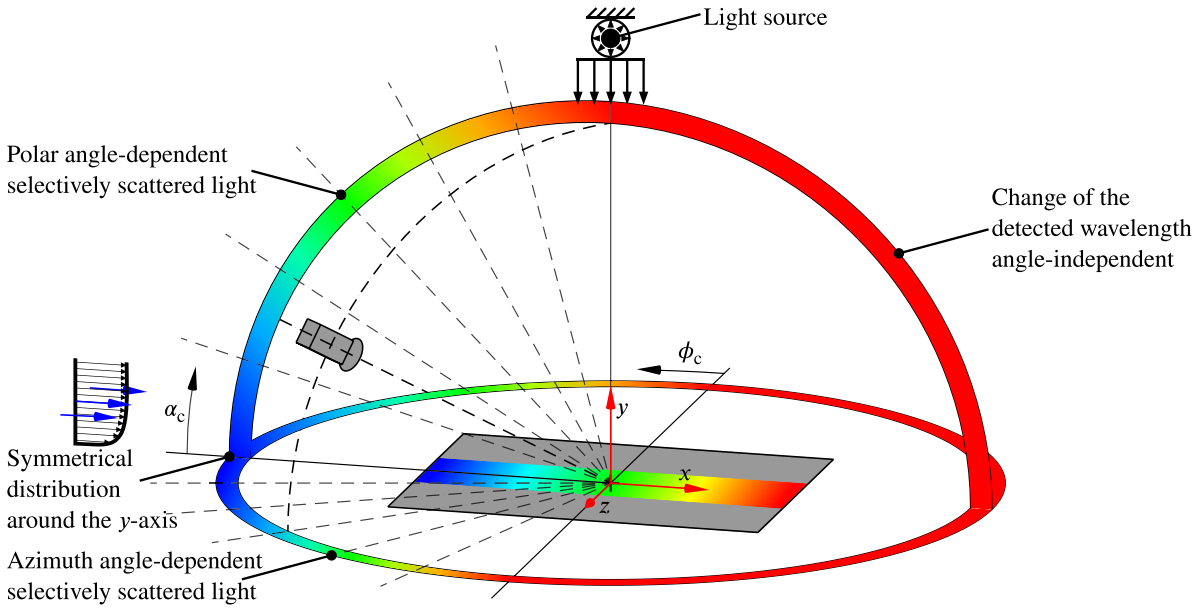

Figure 2. Selectively scattered light, displayed as colors, as a function of azimuth angle ϕ_c and polar angle α_c, illustrated schematically for steady-state flow along a flat plate. The blue arrows are representative of the flow direction with a turbulent velocity profile in between.

I. Calibrate hue H vs. shear stress magnitude τ for a fixed above-plane viewing angle α_c, when the circumferential viewing angle ϕ_c is equal to ϕ_τ, hence $H = H_\tau$.

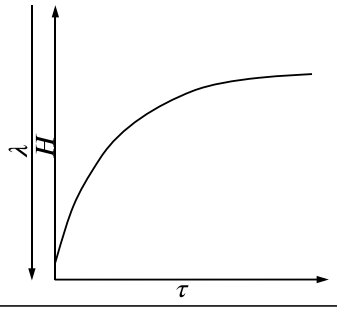

II. For the same above-plane viewing angle, **record** full-surface color images of the approaching flow from m different circumferential viewing angles.

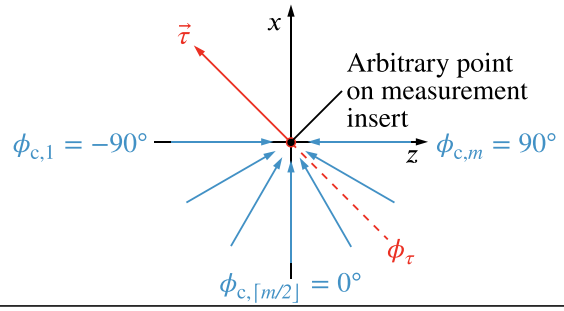

III. Fit recorded hue value over the circumferential viewing angle for each surface point (pixel) with a suitable function, here Gaussian curve, to determine the maximum hue value ϕ_τ and, hence, the **direction**.

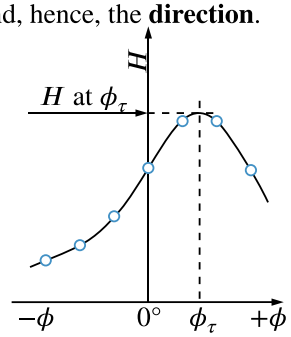

IV. Use the relation between H_τ and τ from the **calibration** (step **I**) to obtain the **magnitude**.

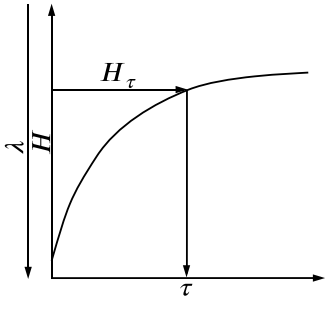

Figure 3. Updated diagnostic principle for measuring wall shear stress vector fields, according to Reda and Muratore [2] adapted by Zhao [13] and Melekidis *et al* [14]. Reproduced with permission from [14]. © 2021 The American Society of Mechanical Engineers.

at a fixed above-plane viewing angle is recorded. There, the minimum dominant wavelength λ_{min} occurs, i.e. the maximum color change from the focal-conic state figure 1(a) to the planar-loaded state figure 1(c) and, hence, the maximum wall shear stress, when the shear vector is aligned with and directed away from the observer. This angular orientation defines the vector orientation ϕ_τ and is therefore referred to as the angle at vector-aligned hue. The values obtained in this way are

required for setting up the calibration curve. For the given setup and fixed above-plane viewing angle, the captured *RGB* values depend at the respective circumferential viewing angle exclusively on the locally induced wall shear stress magnitude and no more on its direction. The recorded color signal can be assigned to the local wall shear stress values performing an *in-situ* calibration. However, additional knowledge on the flow boundaries, e.g. boundary layer height, wall shear stress magnitude, and its distribution is necessary, which has to be determined by means of an additional measurement technique *in-situ*, e.g. Preston tubes or hot wire anemometry [15, 16] or by means of a correlation. The latter is used for the subsequent evaluation of the experimental liquid crystal data presented in this paper. To establish the connection between flow velocity, boundary layer condition, e.g. skin friction coefficient c_f and the prevailing wall shear stress along the liquid crystal layer insert, the empirical correlation by Schlichting *et al* [17], is used in this paper. It can be written as

$$\tau = \frac{1}{2}\rho u_x^2 c_\mathrm{f} \text{ with } c_\mathrm{f} = 2\left[\frac{\kappa}{\ln(\mathrm{Re}_x)} G(\ln(\mathrm{Re}_x))\right]^2. \quad (5)$$

In this context, ρ is the density of the fluid, u_x is the streamwise velocity at position $L_\mathrm{char} = x$, κ is the Karman constant being 0.41, $G(\ln(\mathrm{Re}_x))$ is a function dependent on $\ln(\mathrm{Re}_x)$, with Re being the Reynolds number and assumes the value $G(\ln(\mathrm{Re}_x)) \approx 1.5$ within the Reynolds number range of $10^5 < \mathrm{Re}_x < 10^6$. Based on this correlation, the magnitude of the wall shear stress is quantified, see step **I** in figure 3. The functional dependence of the color signal or the hue and the local wall shear stress magnitude $H_\tau(\tau)$, may then be approximated for a given above-plane viewing angle, by a suitable function that yields the inverse calibration relation $\tau(R,G,B) \equiv \tau(H_\tau(R,G,B))$, see steps **I** and **IV** in figure 3.

In step **II**, for the determination of the wall shear stress vector field of an unknown flow, a number of n images are recorded at each circumferential viewing angle between $-90^\circ \leqslant \phi_\mathrm{c} \leqslant 90^\circ$ at m circumferential positions at constant above-plane viewing angle.

In step **III**, the color values of the number of images converted using a conversion algorithm, see section 3, are approximated by a symmetric function, e.g. a Gaussian distribution or a second-degree polynomial. The maximum of the fitted distribution corresponds to the angle of the local wall shear stress direction, and is referred to as vector-aligned hue.

In step **IV**, the local wall shear stress magnitude is determined from the maximum of the Gaussian distribution H_τ, which corresponds to the minimum dominant wavelength and, thus, the maximum hue value, using the calibration curve from step **I**, see figure 3.

Steps **III** and **IV** are repeated for each image point (pixel) in the region of interest to obtain a full quantitative two-dimensional wall shear stress vector field.

Following the described procedure, it is possible to determine quantitative wall shear stress vector fields. However, a strong limitation immediately becomes apparent in step **I**, which is one of the reasons why liquid crystal diagnostics is not state-of-the-art for determining wall shear stress vector fields and one is still satisfied with correlations that are suitable only to a limited extent or, if the boundary layer thickness admits, with point measurements using conventional measurement techniques. The necessary *in-situ* calibration renders the measurement technique impractical for technically relevant setups with complex secondary flow phenomena, where *in-situ* calibration is usually not possible. In addition, the measurement technique is not robust, since both the magnitude and direction of the wall shear stress are directly dependent on the conversion algorithm used, see step **III**. These conditions result in a long-term goal, namely the creation of a universal and robust calibration for the quantitative determination of the wall shear stress distribution using liquid crystal diagnostics.

3. Status quo: conversion algorithms and calibration

There are *R*-, *G*-, and *B*-based and intensity-based methods for correlating the liquid crystal color signal with a target quantity, see [18]. The former may be advantageous in certain applications. In [19], a higher achievable accuracy is observed in the determination of the color signal-temperature relation with *G*-values compared to *H*-values. In addition, *RGB* values can be processed directly and do not require further conversion. For intensity-based methods, a simple black-and-white camera is sufficient to determine the wall shear stress magnitude. However, with this approach, the liquid crystals have to be in the nematic form. Furthermore, no wall shear stress directions can be obtained. Therefore, these approaches will not be considered or discussed further in the following. Throughout this paper, the hue-based approach proposed by Reda and Muratore [2] as presented in figure 3 is used to determine wall shear stress vector fields. The conversion of the liquid crystal data available in the s*RGB* color space into the intensity-decoupled *HSX* color system is thereby performed by means of a conversion algorithm. In this paper, these algorithms are compared, and their impact on liquid crystal measurement data is examined to derive 'design rules' for the analysis of liquid crystal data and their subsequent comparability. Therefore, the main features of the algorithms are summarized below.

Algorithms for converting *RGB* to *HSX* date back to the 1970s. Tenenbaum *et al* [20] deal with hue-based approaches for the first time and propose a conversion algorithm for interactive scene analysis. Ireland and Jones [21] use the same hue conversion algorithm without any reference or derivation.

A more detailed analysis including improvements is done by Kender [22]. The conversions for the hue, saturation, and normalized color, which are used in the analysis of tricolor natural scenes, are analyzed. All of them have non-removable singularities in which they are unstable. Furthermore, the distribution of the converted values is nonuniform, which is characterized by spurious modes and gaps. Kender quantifies and illustrates these effects. A much faster algorithm for the hue conversion is derived, which contains fewer multiplications

and no square root operations relative to the one introduced by Tenenbaum *et al* [20].

Smith [10] presents a set of alternative models of the *RGB* monitor gamut based on the perceptual variables hue (*H*), saturation (*S*), and value (*V*) and lightness (*L*), respectively. The linear conversion algorithms are fully derived, and their geometric interpretation is provided. Particular attention is paid to a non-trigonometric *RGB*-to-*HSV* transformation pair. Smith states that this is fast, accurate, and sufficient for many applications.

Palus and Bereska [23] compare four *RGB*-to-*HSI* conversion algorithms based on two criteria. On the one hand, the time for execution of the conversion and on the other hand, the number of color objects on the *HS* plane, which they describe as the maximum consistency of the *HS* cluster, are assessed. For the latter, the area is calculated on which the color objects are distributed in the *HS* plane. Palus and Bereska conclude that when comparing the cluster sizes for the examined conversion, the *HSL* [24] color space delivers the best results in terms of object recognition.

The formula originally introduced by Bajón *et al* [25] is different from the one mentioned in [23] called the Bajon transformation. Palus and Bereska simplify the equation in such a way that trigonometric functions are excluded.

Dabiri [26] cites another algorithm and references Kimura *et al* [27] which is the first time a conversion algorithm is used in the literature in connection with liquid crystals. The specification of the hue formula is ambiguous[5] due to vague mathematical notation. Since the publication by Kimura *et al* is only available in Japanese, the most sensible interpretation of the hue is used.

Wang *et al* [28] use a different conversion algorithm and perform experiments on transient heat transfer with liquid crystals. The hue is formulated to be a simple and monotonic function of the liquid crystals' temperature.

Farina *et al* [29] convert the *RGB* data to hue using a different conversion algorithm programmed into their Matrox IM-1280 imaging board [30]. Hay and Hollingsworth note that this definition for the hue is used in a number of imaging devices, but is not mentioned in the colorimetry literature.

In [31], another conversion algorithm is formulated. Hacker and Eaton argue from a physical point of view that a robust definition of the hue should be a monotonic function of temperature. Furthermore, the hue should be invariant to linear changes in illumination intensity and reflection invariant to white light.

Wiberg and Lior [32] examine three different versions of hue conversion algorithms. The recommended algorithm allows for a small error in temperature determination and did not appear previously in the literature.

In [33], another conversion algorithm is formulated. The evaluation of the hue is performed for each pixel, with the minimum and maximum pixel intensity and the minimum saturation as constraints. Only pixels with intensity and saturation above a certain threshold are used to create the calibration curve. Kowalewski [34], similarly to Kodzwa and Eaton [35], takes the saturation as an additional indicator for the selection of the hues to create low-uncertainty calibration curves.

Pratt [36] and Russ [37] each cite another conversion algorithm, but without any explanation of its origin or derivation. However, the algorithm used by Dabiri and Gharib [38] and Dabiri [26] and quoted from Pratt [39] differs from the one they show.

Ziemba and Fornalik-Wajs [40] examine various *RGB*-to-hue conversion algorithms in terms of experimental analysis that satisfy the applicability criteria [40], the suitability for optical temperature measurements [41], and the algorithms' time performance [42]. In addition, the invariability of the hue in the plane containing the intensity axis and the independence of the hue from intensity and saturation are shown.

According to step **I**, see figure 3 in section 2, the characteristic of the calibration curve results directly from the magnitude of the values converted using the researched conversion algorithms. If these are unevenly distributed, their characteristic is discontinuous, or not monotonically increasing, non-physical wall shear stress values may result.

Hay and Hollingsworth [30] make an important contribution to the study of conversion algorithms and the related color signal calibration. They examine various definitions in terms of the effective width of the calibration range and the resulting minimum uncertainty in temperature determination. Three of the approaches studied are based on the hue values, and the fourth is a simple linear regression. To this end, Hay and Hollingsworth calibrate polymer-dispersed chiral-nematic liquid crystals of different temperature ranges. The algorithms used for the conversion are based on different trichromatic representations. Hay and Hollingsworth summarize that the hue definition based on the Nation Television Systems Committee *RGB* triangle turns out to be the best for calibrating the liquid crystals used. The hue definition according to Farina *et al* [29] leads to a strong decrease in the calibratable range due to its definition range, resulting in the largest uncertainties relative to the calibration range. Their preferred conversion algorithm is originally found in Ohta *et al* [43], although it is not clear where it was first introduced.

Park *et al* [44] discuss, among other things, the uncertainties in temperature measurement by thermometry using liquid crystals as seeding. For data processing, the conversion algorithm presented in [38] is used. Specifically, the hue should be insensitive to white light, i.e. insensitive to saturation. Park *et al* note that, in contrast to the hue conversion they used, that of Farina *et al* [29] does not satisfy the illumination invariance criterion. Although the algorithm used in [29] gives slightly better results than their 'standard' hue conversion algorithm [38], both have similar uncertainty levels. This contradicts the findings of Hay and Hollingsworth [30]. This is not elaborated on but is attributed to possible differences in the type of liquid crystal formulations used or their manufacturing.

In summary, the literature research reveals 14 different conversion algorithms, which are further listed in appendix B. Some of them are misquoted from the original source,

[5] On the one hand, the bracketing of the $\cos^{-1}$ is ambiguous. On the other hand, when differentiating between cases, the hue should be subtracted from 2π and not multiplied by it.

definition ranges are insufficiently specified or not specified at all and some are unwittingly used as the result of pre-built functions of commercial codes. Clearly, each of the proposed algorithms meets the requirements of the respective authors to a large extent. However, these strongly depend on the experimental conditions of the respective test rigs and are not universal. In order to establish a universally applicable liquid crystal calibration, it is essential to approach the post-processing of the data, based on the data acquisition under known boundary conditions, fundamentally and consistently. This is why a detailed comparison of the researched conversion algorithms under identical and physical assumptions is mandatory.

4. Evaluation considerations and assumptions

Data $(\bar{R},\bar{G},\bar{B})$ averaged over the integration time of the camera is used to determine a wall shear stress vector field. This signal is locally present at a certain wall shear stress as a function of the observation angle, see equations (3) and (4). Instead of calibrating

$$\tau = f(\bar{R},\bar{G},\bar{B},\vartheta_\mathrm{i},\vartheta_\mathrm{o})\,, \tag{6}$$

it is useful to reduce the *RGB* signal, see section 1, since it contains both intensity (amplitude) and color (wavelength) information, albeit coupled. By means of a suitable conversion algorithm, this information can be largely separated from each other. The result is the hue, saturation, and intensity, which can be illustrated in the form of a double cone, see figure 4.

The point marked with a black cross in the circle on the right hand side is an arbitrary color point. The hue is given as an angle relative to the segment starting from the center of the surface toward the origin (red). Saturation is given by the length of the vector starting at the intersection of the *HS* plane and the intensity axis. The intensity of all colors in each plane is determined by the position of the plane perpendicular to the intensity axis. As described in section 1, the hue is the main quantity to be calibrated for determining wall shear stress. Converting $\bar{R},\bar{G},\bar{B}$ from equation (6) to H leads to the reduced approach

$$\tau = f(H,\vartheta_\mathrm{i},\vartheta_\mathrm{o})\,. \tag{7}$$

It should be noted that the hue is an interpretation of the actual scattered light. Consequently, it represents a parameter that can be designed to meet certain requirements, which is reflected in the number of hue conversion algorithms, see section 3. This means that depending on the definition of the hue, the perceived color change depends not only on the physical scattered light of the liquid crystals, but also on the corresponding color interpretation.

Requirements for a hue conversion algorithm can be derived from this. In physical terms, the hue has to be a monotonic function of the wall shear stress. Furthermore, it should be invariant to linear changes in illumination intensity and different illuminations, provided that the spectral distribution of the light sources is identical. These include, for example, small

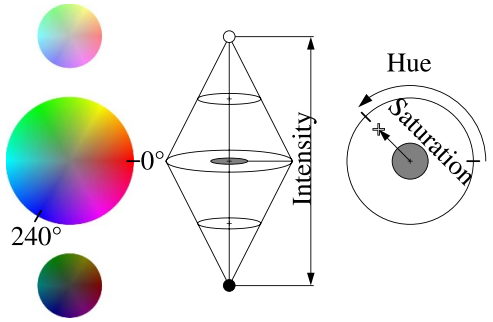

Figure 4. Schematic representation of the hue, saturation, and intensity in the *HSI* color system.

Table 1. Illustration of invariances regarding linear changes in illumination intensity, see equation (8), red crosses on the right hand side, and linear changes in white light, e.g. due to the illumination source or reflections, see equation (9), blue crosses on the left hand side.

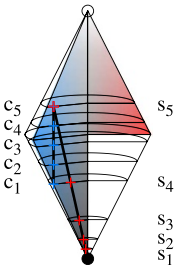

i	1	2	3	4	5
	$s_{i+1} = s_i \times 2$			$s_{i+1} = s_i \times 1.5$	
R	5	10	20	40	80
G	10	20	40	80	160
B	20	40	80	160	240
H			210		
S			50		84.2
X	3.9	7.8	15.7	31.4	62.7
	$c_{i+1} = c_i + 20$				
R	0	20	40	60	80
G	80	100	120	140	160
B	160	180	200	220	240
H			210		
S	100	80	66.7	69.6	84.2
X	31.4	39.2	47.1	54.9	62.7

non-uniformities in illumination and irregular signal amplification across the camera sensor. This results in

$$H(\bar{R},\bar{G},\bar{B}) \equiv H(s\bar{R},s\bar{G},s\bar{B})\,, \tag{8}$$

$$H(\bar{R},\bar{G},\bar{B}) \equiv H(c+\bar{R},c+\bar{G},c+\bar{B})\,, \tag{9}$$

s being an amplification factor and c an arbitrary constant. The invariances to be investigated using the equations are represented by numerical values in table 1 in the *HSI* double cone, see figure 4. To visualize linear changes in illumination intensity, see equation (8), a given starting *RGB* value is multiplied by the introduced amplification factor. Regarding equation (9), an arbitrary constant, i.e. white light, is added to the same given value respectively. The red crosses indicate that when the *RGB* value is changed linearly, both the hue and the saturation are identical, and the intensity doubles. This is in contrast to the addition of white light, e.g. a weak reflection of the same spectral distribution as the actual illumination source. Here, in addition to the intensity, the saturation also changes.

Using the boundary layer theory [45], further requirements can be derived analogously to the wall shear stress characteristic along a flat plate as well as equations (4) and (7). For

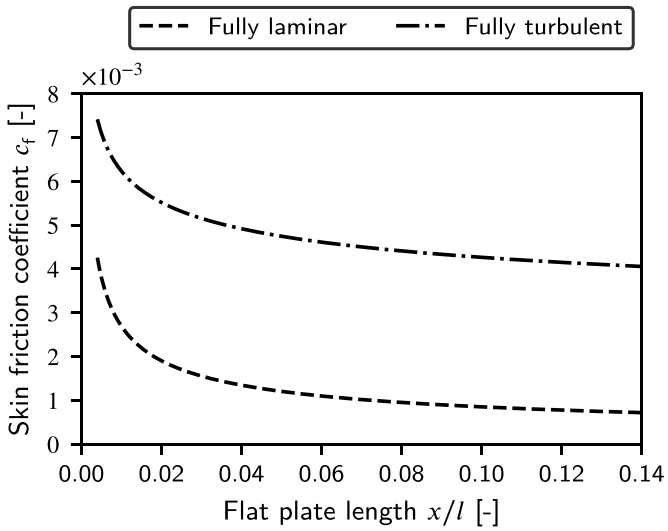

Figure 5. Skin friction distributions along a flat plate, using the correlations by Schlichting *et al* [17].

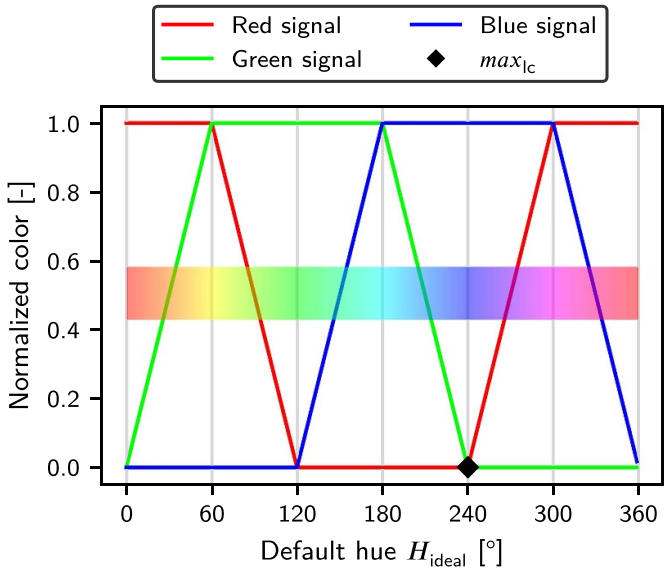

Figure 6. Linearly changing *R*, *G*, and *B* values normalized to 8 bit over the default ideal hue. For better illustration, the resulting *RGB* rainbow is faded in with low opacity.

illustration, the skin friction coefficient c_f using equation (5) is visualized for both fully laminar and fully turbulent, non-accelerated flow, see figure 5. There, the wall shear stress decreases (strictly) monotonically **(A)** and is continuous **(B)**.

Additionally, a synthetic *RGB* dataset is used for the evaluation, specifically a *RGB* rainbow. This can be seen in figure 6. The three normalized curves correspond to the three primaries *R*, *G*, and *B* and are depicted over a default ideal hue H_{ideal}. This starts at $H = 0°$, increases linearly and ends at $H = 360°$, with both values corresponding to the related color red. Green and blue are added and subtracted, respectively, starting at $H = 0°$. The hue is assumed to be approximately a linear homogeneous function of the dominant wavelength, which is the third criterion **(C)**. Wilder and Reda [12] state that this

Table 2. Criteria overview for the evaluation of hue conversion algorithms.

Label	Description
(A)	$f: D \mapsto \mathbb{R}$ $x, y \in D$ with $x < y$, that $f(x) > f(y)$
(B)	Continuous
(C)	$H(\lambda) = m\frac{1}{\lambda}, m \in \mathbb{R}$

holds for $H < 100°$, although it is not elaborated. The black marker in figure 6 indicates the shortest detectable wavelength in the scattered light of liquid crystals, which is pure blue at $H = 240°$, see figure 4, and is also mentioned in the literature, e.g. [28]. Due to this limit, the relevant range for the following evaluation of the conversion algorithms is $H = 0°$–$240°$. The criteria introduced are summarized in table 2 as an overview.

5. Resulting conversion algorithms and discussion

The color values of the *RGB* rainbow, see figure 6, are converted using the conversion algorithms listed in tables B1–B4, see appendix B. For evaluation, the criteria formulated in table 2, see section 4, are used.

To illustrate the wide range of the resulting hues of the different conversion algorithms, the calculated hue *H* is displayed over the default ideal hue H_{ideal} which serves as a reference, see figure 7. This reference fulfills criteria **(A)**, **(B)**, and **(C)**. Based on the data series shown, it is observed that using a certain conversion algorithm may lead to completely different results for the same input *RGB* data. Furthermore, the calculated hues are not limited to $H = 0°$–$360°$, which results in a calculated hue range of approximately $H = -100°$–$360°$. For simplicity, the conversion algorithm of each author, see figure 7, is mentioned in the following with, e.g. (1) in the text.

Examining the data series, it is evident that some of them do not fulfill the criterion of a monotonically increasing **(A)** and a continuous **(B)** curve characteristic. The values converted using (2) and (3), (5–9 and 14), see tables in appendix B, show a step change. Conversion algorithm (4) is undefined between approximately $H = 60°$–$100°$ and $240°$–$280°$. Consequently, the use of this algorithm may lead to unassignable wall shear stresses. The missing monotonically increasing characteristic of the mentioned conversion algorithms would further cause that several wall shear stresses could be assigned to one hue value. Considering a generally valid calibration function and an unambiguous assignment, this is not reasonable. Algorithms (5–8) show the characteristic curve shape of an arctan around $H = 90°$ along the abscissa. Conversion algorithms (6–8) additionally exhibit an offset, both along the abscissa toward approximately $H = 130°$ respectively $H = 150°$ and in the direction of negative values along the ordinate toward approximately $H = -35°$, $-40°$, and $-60°$. Taking into account the formulated criteria, see table 2, the algorithms (2–4 and 5–8) are not further assessed. The hue values according to (9) and (14) exhibit discontinuity in the wavelength (hue) range of the liquid crystals.

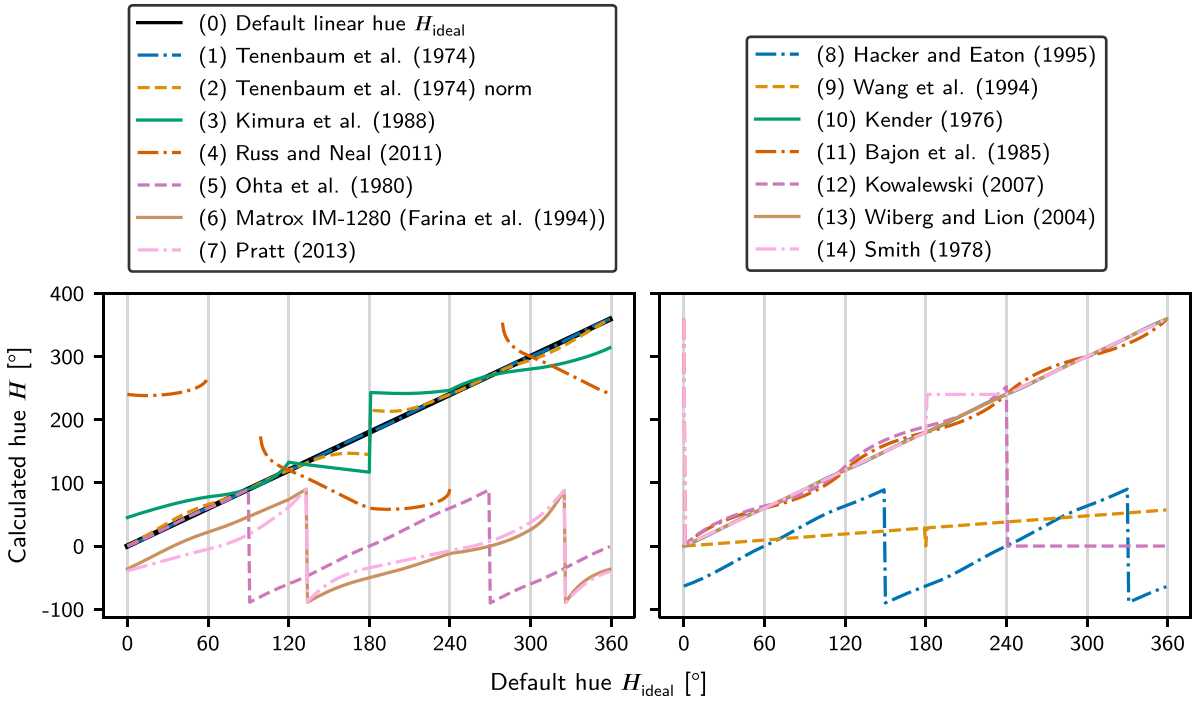

Figure 7. Hue values calculated from the normalized *RGB* values using different conversion algorithms.

However, based on in-house investigations as well as published calibration curves of other authors, it is found that a minimum hue of $H = 0°$ can neither be achieved in the focal-conic nor in the planar unloaded state, see figure 1. This may be due to the substrate on which the liquid crystals are sprayed or the thickness of the liquid crystal coating and its absorption properties. From this and the shortest detectable wavelength in the scattered light of liquid crystals, i.e. the maximum hue value, see section 4, a relevant hue range of $H = 5°$–$240°$ results, within which the conversion algorithms must satisfy the specified criteria. Consequently, the hue values according to (9) and (14) are still considered for reasons of the wall shear stress ranges achievable in an experiment, although they exhibit discontinuity in the wavelength (hue) range of the liquid crystals.

For further evaluation, the difference to the ideal preset hue $\Delta H = H_{ideal} - |H|$ of the conversion algorithms from the first iteration are displayed in the corresponding value range, see figure 8. Assuming that the hue is a linear function of wavelength, further conversion algorithms can be removed from consideration. Conversion algorithm (9) has a low sensitivity. The calculated hue changes in the range of about $H = 0°$–$60°$. This can also be seen from the small slope of data series (9) in figure 7 and the large slope in figure 8, respectively. Data series (12), in contrary, has a higher sensitivity, which can be seen from the slightly increasing negative values it assumes with increasing hue, see figure 8. Using the conversion algorithm, Kowalewski [34] achieves that the calculated hue at a given $(R, G, B) = (0, 0, 1)$, ergo $H_{ideal} = 240°$ already assumes a calculated value $H = 252°$. Since both criteria **(A)** and **(B)** are met and there is a large slope, conversion algorithm (12) is retained for further evaluation. Data series (1, 10 and 11) are periodic, oscillating around $\Delta H = 0°$

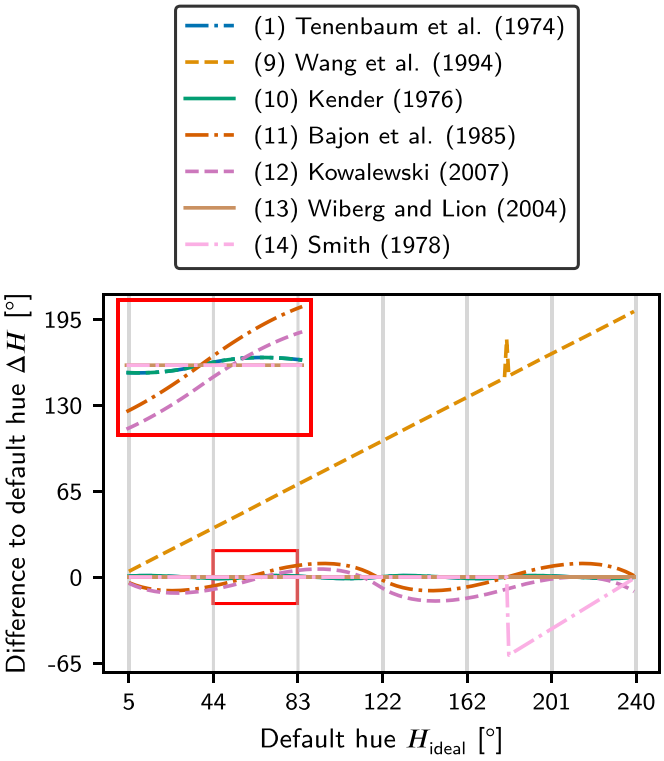

Figure 8. Calculated hue value differences relative to default hue values.

along the abscissa, see figure 8. Data series (12) also oscillates around the abscissa, but drifts toward negative values as the hue increases, see figure 8. The hue changes in the interval $[-1, +1]$ for (1) and (10) and $[-10, +10]$ for (11), respectively.

Table 3. Preliminary evaluation of the preselected conversion algorithms.

Number	Property		
	Characteristic	Interval ΔH	Slope
(1)	Periodic	$\approx[-1,+1]$	1
(10)	Periodic	$\approx[-1,+1]$	1
(11)	Periodic	$\approx[-10,+10]$	1
(12)	Aperiodic	—	1.05
(13)	Linear	—	1
(14)	Linear	—	1

Data series (13) and (14) are linear, with (14) being discontinuous from $H > 180°$.

From this preliminary evaluation it follows that conversion algorithms (1 and 10–14) are suitable for liquid crystal image analysis based on the formulated criteria and assumptions. This is summarized in table 3. Supplementarily, the findings of the numerical analysis and the evaluation regarding the criteria are listed in table B5.

5.1. Illumination invariance of selected algorithms

Based on the previous evaluation, the illumination invariance, see section 4, of the preselected conversion algorithms is now discussed from a strictly numerical point of view. Conversion algorithms (1, 10 and 14) are variant to the illumination intensity, see equation (8). In, e.g. (1), the *RGB* values within the $\cos^{-1}$ may be expressed by the intensity I, see table B1, where $I = \frac{R+G+B}{3}$ and thus the hue depends directly on the illumination intensity. Further inspection of (10) and (14) reveals a direct dependence on intensity. In contrast, conversion algorithms (11–13) are invariant to illumination intensity.

Moreover, it is found that the hue conversion algorithms (1, 10, 11 and 14) are invariant to different illuminations, assuming the spectral distribution of the illumination sources being identical, e.g. collimated and diffuse light, respectively, see equation (9). Conversion algorithms (12) and (13) are, in contrast, illumination source variant. Only one of all presented conversion algorithms satisfies both criteria, namely (11) by Bajón *et al* [25].

The theoretical findings are illustrated by applying the selected conversion algorithms to experimental data. For this purpose, four images of a flat plate coated with liquid crystals are acquired at certain integration times, see figure 9, using the calibration setup presented by Melekidis *et al* [14]. The camera is set to $\alpha_c = 40°$ and the illumination is perpendicular to the coated surface, see figure 2. Throughout the experiment, the liquid crystals are not subject to any wall shear stress and are thus in the focal-conic state, see figure 1(a). Extraneous light falling on the liquid crystal coating or reflections from mounted components are avoided by covering the surrounding area with deep black curtains. For data acquisition, a *Nikon D7200* is used. To investigate the impact of illumination intensity, images are taken at different integration times. These are $t = 0.125, 0.25, 0.5$, and 1 s. The integration time is chosen as a parameter for simplicity, since it can be changed more easily and reproducibly in contrast to the intensity of the illumination. To investigate the impact of collimated and diffuse light, a diffusing screen is placed in front of the collimator. This ensures that the spectral distribution of the illumination source remains the same, allowing the invariance to linear changes in white light to be investigated. During the measurements to investigate the two criteria, see equations (8) and (9), both the camera settings and the illumination source remain the same. Only the integration time is changed.

For the conversion of the four samples of a flat plate, each recorded at a different integration time, the conversion algorithms (12) and (13) are used. The resulting hue values and their normalized number probability density function (pdf) is displayed over the respective integration time, see figure 9. The size of the region of evaluation, see black frame on the left hand side in figure 9, is always $z \times x = 160\,\text{px} \times 600\,\text{px}$ for all shown figures. The images illustrated and evaluated are compressed image formats (JPEG) and are not post-processed, i.e. no filters/corrections are applied. The acquired images are converted with conversion algorithms (12) and (13) at the respective integration times. The color map used corresponds to the calculated hue. Photographs appear basically very homogeneous for each integration time, which is also confirmed by the qualitative low standard deviations. However, toward higher integration times and especially at $t = 0.5\,\text{s}$, a slight hue gradient along the x-coordinate is noticeable, see figure 9. This is underlined by the calculated standard deviation, see table 4. The exact values for the quantities calculated with the used conversion algorithms are listed in table 4. Based on the numerical examination of the conversion algorithms according to equation (8), it is expected that despite different integration times and thus different intensities, the hue values calculated with (12) and (13) are the same. By calculating the mean value of all hues $\bar{H}$ of the region of evaluation and the standard deviation σ, it is apparent that the mean hue value increases with increasing intensity. The relative deviation of the hues from the mean value σ_{rel} is in the order of 2%–6% for the images converted with (12) and about 4%–9% for those converted with (13). The data listed in table 4 allows the conclusion that the hue distributions show differences both within a dataset evaluated with one conversion algorithm and between datasets evaluated with different conversion algorithms. For instance, the maximum deviation of the hue at an eight times higher integration time and thus a theoretically eight times higher intensity[6] is 24.5° for (12) and 30.5° for (13). Moreover, the data converted with (12) exhibits absolute higher hue values for all intensities relative to values converted with (13). This is also evident from the data series shown in figure 7 for the range 0°–60°. For this range, hues are higher as a result of the periodic characteristic around the default linear hue data series. From the pdf, it is found that although the hue values deviate around a certain mean value, the standard deviation is small. This small but still existing deviation around the mean value is attributed to the liquid crystal coating that is applied to the measurement insert

[6] This assumption is valid exclusively for an ideally linearly behaving sensor.

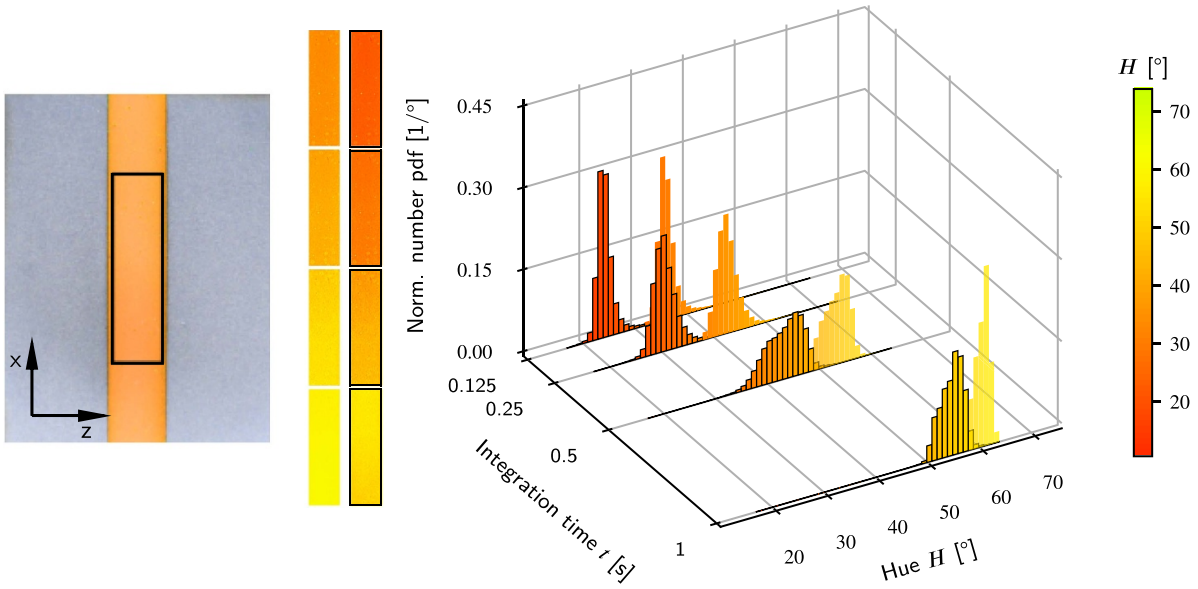

Figure 9. Impact of illumination on data from a liquid crystal-coated (focal-conic state) flat plate at different integration times $t = 0.125, 0.25, 0.5$, and 1 s (intensity increases with increasing integration time from top to bottom) under collimated light according to equation (8) using conversion algorithm (12), not edged, and (13), edged, in black. The black frame on the liquid crystal measurement insert represents the region of evaluation.

using an artist airbrush. The entire coating is very uniform due to the automatic coating process, however, small sprinklers are visible in the region of evaluation. Within this imperfection caused by the coating process, significantly higher hue values[7] are calculated for these pixels, which in turn increase the mean value of the hue. Furthermore, it can be seen from figure 9 and table 4 that the standard deviation slightly increases with increasing integration time (intensity) and drops for $t = 1$ s. To explain this characteristic, the average ratio of the intensity $\bar{X}$ and the $\bar{R}$, $\bar{G}$, and $\bar{B}$ values for the region of evaluation are calculated. This is performed for images with consecutive integration times, e.g. $\frac{\bar{X}_{0.25\text{ s}}}{\bar{X}_{0.5\text{ s}}} \equiv \cdots$. For an approximately linear camera sensor, $\frac{\bar{X}_t}{\bar{X}_{2t}} \equiv \frac{\bar{R}_t}{\bar{R}_{2t}} \equiv \frac{\bar{G}_t}{\bar{G}_{2t}} \equiv \frac{\bar{B}_t}{\bar{B}_{2t}}$ must apply. The ratios for the images converted with (12) are listed in table 5. The calculated ratios of $\bar{R}$, $\bar{G}$ and $\bar{B}$ are different for one integration time ratio, but similar for exposures at different integration time ratios. This is also the case for the intensity. The average deviation $\overline{RGB}$ relative to $\bar{X}$ is in the range of about 5%–10% for all integration time ratios. Contrary to the numerical investigation of (12) and (13), the used conversion algorithms are not illumination-invariant to different intensities. As shown, the increasing mean hue values may be attributed to the nonlinearity of the camera sensor or the use of compressed image formats, which may lead to the observed deviations between datasets converted with the same conversion algorithm but at different integration times.

In figure 10, the calculated hues of the liquid crystal coating for collimated and diffuse light are illustrated, using conversion algorithms (1) and (10) to demonstrate the illumination invariance according to equation (9). Based on the numerical examination of the conversion algorithms according to equation (9), it is expected that despite collimated or diffuse light, the resulting hue values calculated with (1) and (10) are the same. Based on figure 10, this cannot be confirmed. Instead, the hues are different for the same image at the same integration time. It is observed that the mean hue value is

[7] They result from the accumulation of liquid crystal mixture at the nozzle outlet due to the temperature drop and the related decrease in viscosity during coating.

Table 4. Mean value and standard deviation of the normalized number pdf for conversion algorithms (12) and (13) using collimated light.

		t (s)			
Number	Quantity	0.125	0.25	0.5	1.0
(12)	$\bar{H}$ (°)	34.8	41.2	51.7	59.3
	σ (°)	1.9	2.3	2.6	1.3
	σ_{rel} (%)	5.5	5.5	5.0	2.1
(13)	$\bar{H}$ (°)	22.9	29.3	41.9	53.4
	σ (°)	1.9	2.5	3.5	2.1
	σ_{rel} (%)	8.2	8.6	8.3	4.0

Table 5. Intensity $\bar{X}$ and $\bar{R}$, $\bar{G}$ and $\bar{B}$ ratios to account for the linearity of the camera sensor. The values are calculated for conversion algorithm (12).

	Ratio			
t	$\bar{X}$	$\bar{R}$	$\bar{G}$	$\bar{B}$
$\frac{0.125\text{ s}}{0.25\text{ s}}$	0.89	0.96	0.77	0.67
$\frac{0.25\text{ s}}{0.5\text{ s}}$	0.90	1.00	0.79	0.75
$\frac{0.5\text{ s}}{1\text{ s}}$	0.90	1.01	0.87	0.68

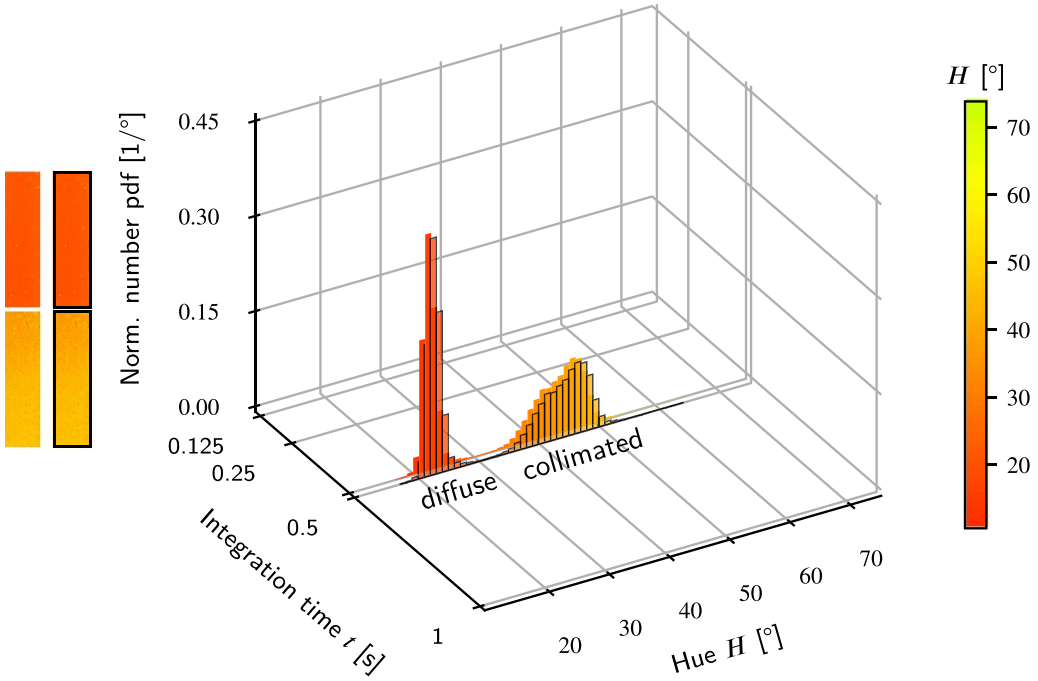

Figure 10. Impact of illumination on data from a liquid crystal-coated (focal-conic state) flat plate at a integration time $t = 0.5$ s under diffuse and collimated light according to equation (9) using conversion algorithm (1), not edged, and (10), edged, in black. The histograms are on top of each other for both diffuse and collimated light, but are displayed with a spacing in between for better depiction.

Table 6. Mean value and standard deviation of the normalized number pdf for conversion algorithms (1) and (10) at $t = 0.5$ s.

		Light source	
Number	Quantity	Diffuse	Collimated
(1) and (10)	$\bar{H}$ (°)	21.4	42.8
	σ (°)	1.5	3.7
	σ_{rel} (%)	7.2	8.6

Table 7. $\bar{R}$, $\bar{G}$ and $\bar{B}$ differences to account for the linearity of the camera sensor. The values are calculated for conversion algorithm (1) at $t = 0.5$ s.

	Difference		
	$\bar{R}$	$\bar{G}$	$\bar{B}$
|diffuse − collimated|	0.20	0.43	0.28

lower for diffuse than for collimated light. The desired strong drop in intensity is achieved by attaching a diffusing screen in front of the illumination source. Again, it turns out that with increasing intensity, the standard deviation of the hue also increases. Moreover, the converted values using conversion algorithms (1) and (10) are approximately identical. This is reasonable considering the two overlapping linear data series, see (1) and (10) in figure 7. The exact values for the quantities calculated with these conversion algorithms are listed in table 6. To further elaborate on the illumination invariance according to equation (9), namely whether the white component of light is evenly distributed among the components R, G, and B for the same illumination source and consequently the same spectral distribution, the absolute mean value of the difference between the individual color components is calculated, e.g. $|\bar{R}_{\text{dif}} - \bar{R}_{\text{col}}|$. The resulting quantities are listed in table 7. The highest value is calculated for the green component, which is about two times larger than the R and B. This is reasonable as green pixels are available twice as often on the Bayer filter of the camera sensor compared to red and blue pixels. The results clearly indicate that despite the invariant conversion algorithm to white light, see equation (9), no invariant hue values can be computed from the experimental data. Apart from the result of the investigation regarding the illumination invariance according to equation (9), the case of incident extraneous light or reflections on the measuring surface is rather the exception for experiments in the laboratory. This is why the illumination invariance to linear changes in illumination intensity, see equation (8), is more relevant compared to the reflection invariance with respect to white light from an illumination source with the same spectral distribution, see equation (9).

Finally, in figure 11, data to analyze fully illumination invariance are presented. For examination, conversion algorithm (11) is used. Based on the numerical examination of the conversion algorithm (11), it is expected that full illumination invariance is achieved using (11) despite different intensities, see equation (8), and amount of white light, see equation (9). This is approximately true for images taken under diffuse light at different integration times, see figure 11, not edged images. For both $t = 0.25$ and 0.5 s, the hue value

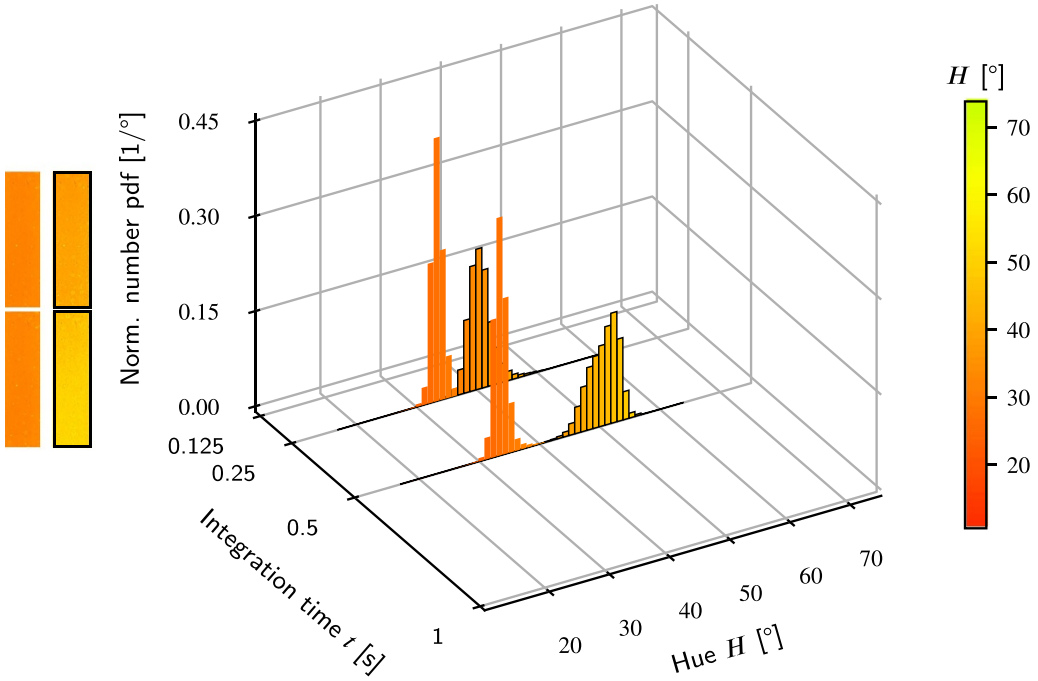

Figure 11. Impact of illumination on data from a liquid crystal-coated (focal-conic state) flat plate at different integration times $t = 0.25$ and 0.5 s (intensity increases with increasing integration time from top to bottom) according to equations (8) and (9) using conversion algorithm (11). Histograms that are not edged represent hue values with diffuse illumination, those edged, in black with collimated illumination.

Table 8. Mean value and standard deviation of the normalized number pdf for conversion algorithm (11).

		Light source	
t	Quantity	Diffuse	Collimated
0.25 s	$\bar{H}$ (°)	32.2	39.3
	σ (°)	1.2	2.2
	σ_{rel} (%)	3.9	5.5
0.5 s	$\bar{H}$ (°)	32.3	49.2
	σ (°)	1.4	2.5
	σ_{rel} (%)	4.4	5.0

Table 9. Intensity $\bar{X}$ and $\bar{R}$, $\bar{G}$ and $\bar{B}$ ratios and differences to account for linearity of the camera sensor. The values are calculated for conversion algorithm (11).

	Ratio			
t	$\bar{X}$	$\bar{R}$	$\bar{G}$	$\bar{B}$
$\left.\frac{0.25\,\text{s}}{0.5\,\text{s}}\right\|_{\text{dif}}$	0.61	0.69	0.58	0.29
$\left.\frac{0.25\,\text{s}}{0.5\,\text{s}}\right\|_{\text{col}}$	0.88	1.00	0.79	0.75
	Difference			
$\lvert\text{diffuse} - \text{collimated}\rvert_{0.25\,\text{s}}$	—	0.44	0.42	0.29
$\lvert\text{diffuse} - \text{collimated}\rvert_{0.5\,\text{s}}$	—	0.20	0.43	0.28

is 32.2° and 32.3°, respectively, with a small standard deviation 1.2° and 1.4°, see table 8. In contrast, the change in hue value for collimated light from $t = 0.25$ and 0.5 s is of the same order of magnitude as for conversion algorithm (12), see table 4. Again, the standard deviation increases with increasing intensity, see table 4. Considering equation (9), which also has to be satisfied using conversion algorithm (11) by [25], a distinct difference is observed for diffuse and collimated light at identical integration times $t = 0.25$ s and $t = 0.5$ s, respectively, with respect to the hue value. The behavior of the quantities is the same as in figure 10, namely that both the hue and the standard deviation increase. The exact values for the quantities calculated with conversion algorithm (11) are listed in table 8. To explain the calculated quantities, the ratios as well as the differences of the used values are applied, see table 9. Comparing the ratios for diffuse and collimated light confirms the previously observed non-linearity of the camera sensor when changing the intensity (integration time). The equal distribution of white light on the individual color channels with the same illumination source is also not given for both integration times examined.

Although based on theoretical considerations, it has been demonstrated numerically, that there are conversion algorithms that are invariant to certain requirements, for example, the illumination intensity, see equation (8), or the amount of white light, e.g. reflections with the same spectral distribution as the illumination source, see equation (9), or a combination of both, this invariance is not preservable in experimental data. This may be due to the non-linearity of the camera sensor, the use of already processed, compressed image formats, or the non-ideally adjustable experimental parameters leading to this result. To highlight the effects of the

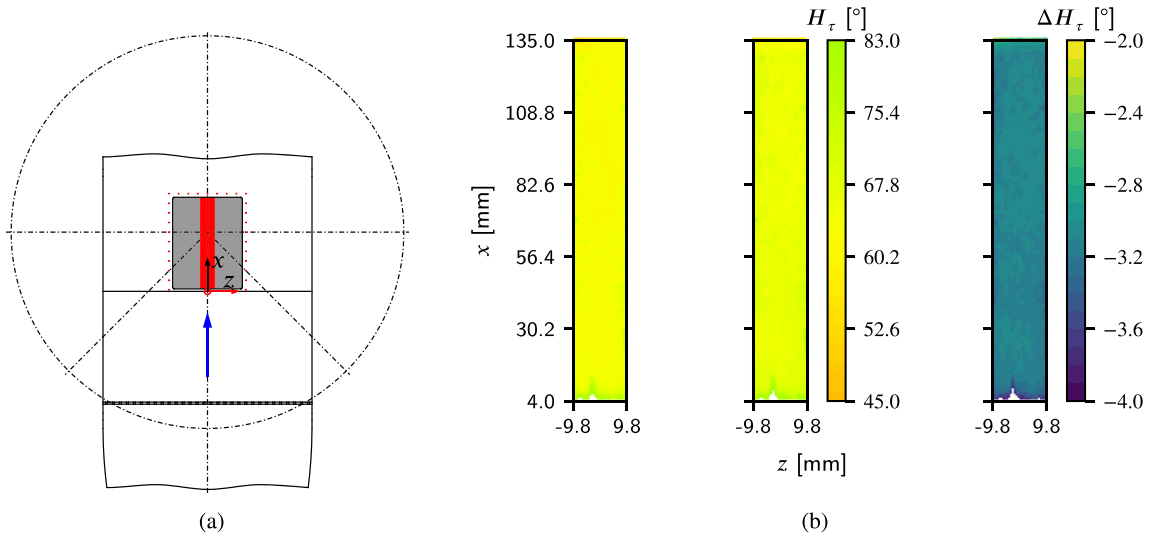

Figure 12. Flow field distributions of cropped and geometrically converted liquid crystal images derived from five recordings at different circumferential viewing angles, fixed above-plane viewing angle $\alpha_c = 25°$, and an approaching flow from bottom to top. The red square in (a) represents the region of evaluation. (a) Adapted test section: Region of evaluation according to [14]. Reproduced with permission from [14]. © 2021 The American Society of Mechanical Engineers. (b) Uncalibrated wall shear stress field using (11) left, (12) right, and $\Delta H_\tau = H_{\tau,(11)} - H_{\tau,(12)}$.

differently performing conversion algorithms on experimental data, conversion algorithms (1), (11), and (12) are used in the following.

5.2. Impact of algorithms on hue distribution

Synthesizing on the presented investigations, the influence of the evaluated conversion algorithms is examined using another experimental dataset. The liquid crystal layer is now, in contrast to the studies in section 5.1, subjected to a stationary flow and is consequently in the planar (loaded) state, see figure 1(c). The relations shown in sections 1 and 2 result in a color spectrum that can be evaluated using the approach by Reda *et al* see figure 3, as well as the evaluated conversion algorithms (11) and (12) with the conversion algorithm (11) by Bajon *et al* being the favorable one. In the following, this is referred to as the 'standard case'. Algorithm (11) is selected since it is the only algorithm that satisfies both criteria and provides approximately equal hue value distributions at different integration times. Algorithm (12), in contrast, is selected since it is closer to an experimental setting compared to conversion algorithms (1) and (10) with regard to linear changes in illumination intensity, since extraneous light incidence or reflections can be largely avoided in laboratory tests.

Using the generic flat plate test section presented by Melekidis *et al* [14], the liquid crystal data is acquired. Appropriate flow boundary conditions can be accurately set there. These include a well-known turbulence intensity of $Tu = 6.40\%$, a fully adjacent boundary layer of known height, and measured velocity and temperature profiles. Based on the distance from the measurement insert's leading edge the calculated Reynolds number is within $Re_x = 7.3 \times 10^4$–2.3×10^5. For additional information on the operating point stability, etc [14] is recommended. The resulting uncalibrated wall shear stress field for the set parameters is shown in figure 12. There, the differences regarding the uncalibrated wall shear stress magnitude is visualized using the same dataset for evaluation. The differences are caused by the conversion algorithms used, see figure 12(b). The calculated hue for the conversion case (12) is on average $H_\tau \approx 3°$ above the mean calculated hue value relative to the standard case according to Bajon *et al*. This is plausible and can be explained by the curve characteristic illustrated in figures 7 and 8. The maximum hue difference $\Delta H_\tau = H_{\tau,(11)} - H_{\tau,(12)}$ is calculated to $H_\tau \approx 4°$ and is present in the area of the measurement insert leading edge, where the highest hue values are also located.

In the next step of the Reda *et al* calibration procedure, the calibration curve would be generated from the hue data shown. As already indicated by means of ΔH_τ, these would obviously be different and consequently lead to different wall shear stress distributions, although the dataset is the same. From the data shown, it appears that the mutual dependencies between the integration time, the type of illumination (diffuse/collimated), and the state in which the liquid crystals are examined (unloaded/loaded) are still an open issue and require further investigation. Furthermore, it is becoming apparent that the determination and subsequent comparability of wall shear stress data are far from trivial, which is why this will be discussed in more detail in future studies.

6. Guidelines on suitable conversion algorithms and liquid crystal data acquisition

The quantification of wall shear stress and its direction is challenging, as these quantities cannot be directly detected and

measured. Consequently, calibration is indispensable. Liquid crystal diagnostics can be used to provide data with high resolution and low error, provided the relevant influencing parameters are known, and the calibration is performed correctly. Errors may arise from the flow, the recording system, and the data processing. For the latter, a conversion algorithm is required, which has a huge influence on the derived wall shear stress vector field. These conversion algorithms are numerous in the literature and are investigated in this paper for their suitability for experimental liquid crystal data and their influence under certain assumptions.

From literature research, a total of 14 different conversion algorithms emerged, more than half of which do not meet the required criteria and are consequently unsuitable for the conversion of liquid crystal data. Based on this, a preselection of the conversion algorithms was made with respect to invariance to linear changes in illumination intensity, see equation (8), and reflection invariance to white light from the same illumination source, see equation (9), to reduce the number of conversion algorithms. Two numerically invariant conversion algorithms result with respect to the illumination intensity, namely that by Kowalewski (12) and by Wiberg and Lion (13). The two conversion algorithms according to Tenenbaum *et al* (1) and Kender (10), in contrast, are numerically invariant with respect to white light. Only one conversion algorithm satisfies both requirements, that by Bajon *et al* (11).

To further investigate these numerically studied algorithms, they are applied to an experimental liquid crystal dataset, consisting of four recordings at different integration times in the focal-conic state. For short integration times, an approximately sharp hue value distribution with a low standard deviation is identified, independently of the conversion algorithm used. The standard deviation increases with increasing integration time. Likewise, the mean value of the hue distribution tends to increase with increasing intensity. The same behavior is observed under diffuse illumination, with lower hue values relative to data acquired under collimated illumination. The large differences in the mean hue values of up to approximately $\bar{H} = 12^\circ$ of the same data at the same integration time calculated using different conversion algorithms highlight the importance of using a suitable conversion algorithm for data processing. The conversion algorithm (11) by Bajon *et al* [25] is suitable for this purpose, showing the best performance for both numerical and experimental data. In general, however, it must be stated that despite the numerically shown illumination invariance of some conversion algorithms with respect to equation (8) or (9), and equations (8) and (9), respectively, this cannot be observed within the experimental liquid crystal data examined. The differences observed may be attributed to the non-linearity of the camera sensor, to the use of processed, already compressed image formats, or the non-ideally adjustable experimental parameters.

From the investigations carried out, the following recommendations and statements on liquid crystal measurements are derived:

- Use the same algorithm to convert the *RGB* data, preferably that by Bajon *et al*.
- Use the same camera settings and illumination source.
- Short integration times, e.g. 0.25 and 0.5 s, result in smaller standard deviation values compared to longer ones, which is preferable if the illumination intensity allows it.
- Diffuse illumination may be beneficial in terms of standard deviation in the unloaded state.

Summarizing the results, the studied illumination variance is inevitably accompanied by a dependence on the recording device and consequently a variance of the recording device. The use of different recording devices can therefore also lead to different results. Thus, in addition to the experimental setup, the illumination, the recording device used, and the presets set are of particular importance. Furthermore, besides a sensor signal linearization, the processing of (proprietary) uncompressed data that depends exclusively on the selectively scattered light of the liquid crystals is recommended. Further attention should be paid to the in-camera raw signal processing and subsequent data preparation. These measures could form the basis for the acquisition of illumination- and camera-invariant liquid crystal data, which can then be evaluated with the recommended conversion algorithm and will be part of future studies.

Data availability statement

The data that support the findings of this study are available upon reasonable request from the authors.

Acknowledgments

The authors wish to thank Karla Herrera, Anna Keim, Oliver Rousseau, Marcus Ebert, and Lorenz Weber for supporting the data acquisition activities carried out at the Institute of Thermal Turbomachinery. Furthermore, the authors acknowledge support from LCRHallcrest Ltd for providing a sample of BN/R50C and the reviewers for their valuable comments, which led to improvements in the manuscript. The responsibility of the content lies solely with the authors.

Appendix A. Liquid crystal classification

Note that in the literature, the terms ‘cholesteric’ and ‘chiral-nematic’ are often used synonymously. Therefore, depending on the constituents of the chemical compound,

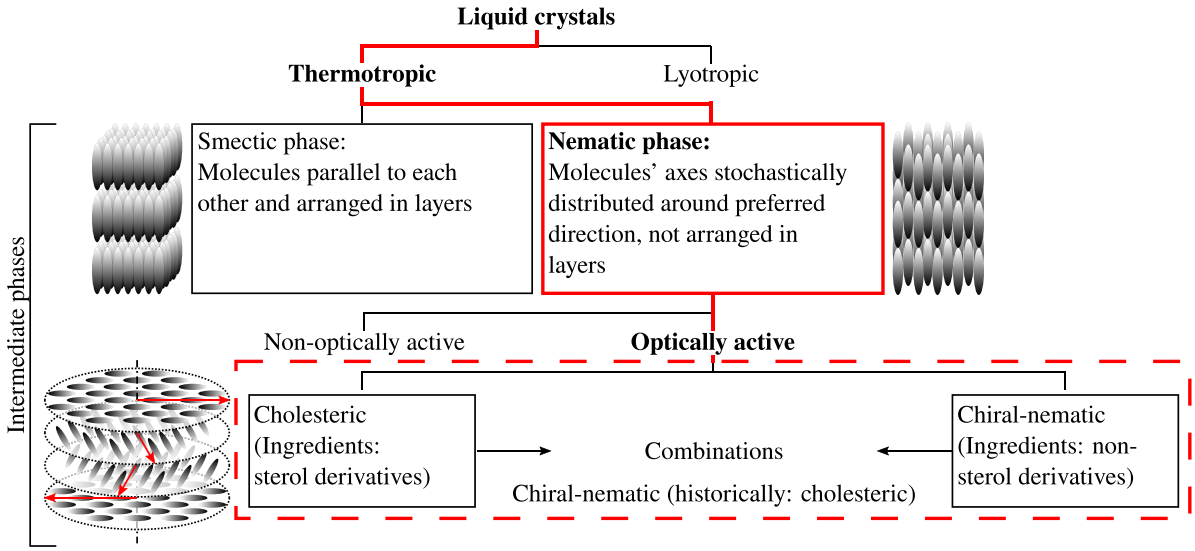

Figure A1. Schematic representation of the classification of liquid crystals according to [46]. In liquid crystal diagnostics, thermotropic liquid crystals of the optically active nematic phase are utilized.

a differentiation is made between the cholesteric and the chiral-nematic phase, although combinations of both are possible [46]. 'Cholesteric' in the following refers to the cholesterol or other sterol-based compounds on the basis of which the optical behavior of the cholesteric phase was first observed [5].

In contrast, the chiral-nematic phase does not explicitly consist of sterol-based substances. However, both phases have the same optical properties and the same chiral-nematic structure. The latter is characterized by the twisted helix structure along which the direction of the long axis of the molecules changes between each molecular plane. Within a plane, the molecules are nematically aligned. The structure described can be seen in figure A1. The liquid crystals used at the Institute of Thermal Turbomachinery contain non-sterol-based compounds and therefore belong to the category of the chiral-nematic phase.

Appendix B. Conversion algorithms

Table B1. Available *RGB*-to-hue conversion algorithms[a,b,c,d] toward quantitative wall shear stress measurements, part (1/5).

Number	Citation	Algorithm (abbr.)	Hue
(1)	Tenenbaum *et al* [20]	Tenenbaum	$H=\begin{cases}\theta, & \text{if } G'\geqslant B'\\ 2\pi-\theta, & \text{if } G'<B'\end{cases}$ with $\theta=\cos^{-1}\left(\frac{\frac{1}{2}\left[(R'-G')+(R'-B')\right]}{\sqrt{(R'-G')^2+(R'-B')(G'-B')}}\right)$
(2)	Tenenbaum *et al* [20]	Tenenbaum	$H=\begin{cases}\theta, & \text{if } G\geqslant B\\ 2\pi-\theta, & \text{if } G<B\end{cases}$ with $\theta=\cos^{-1}\left(\frac{2R-G-B}{\sqrt{6\left[\left(R-\frac{1}{3}\right)^2+\left(G-\frac{1}{3}\right)^2+\left(B-\frac{1}{3}\right)^2\right]}}\right)$
(3)	Kimura *et al* [27]	Kimura	$H=\begin{cases}\theta, & \text{if } g\geqslant b\\ 2\pi-\theta, & \text{if } g<b\end{cases}$ with $\theta=\cos^{-1}\left(\frac{2r-g-b}{\sqrt{6S}}\right)$
(4)	Russ [37]	RN	$H=\begin{cases}\theta & \text{if } G\geqslant R\\ 2\pi-\theta, & \text{if } G\leqslant R\end{cases}$ with $\theta=\cos^{-1}\left(\frac{2B-G-R}{2\sqrt{(B-G)^2+\frac{B-R}{G-R}}}\right)$
(5)	Ohta *et al* [43]	Ohta	$H=\tan^{-1}\left(\frac{\sqrt{3}(G-B)}{2R-G-B}\right)+\theta$ with $\theta=\begin{cases}0, & \text{if } 2R\geqslant G+B\\ \pi, & \text{if } 2R<G+B\end{cases}$
(6)	Matrox IM-1280 [29]	Farina	$H=\tan^{-1}\left(\frac{V_2}{V_1}\right)$
(7)	Pratt [36]	Pratt	$H=\tan^{-1}\left(\frac{V_2}{V_1}\right)$
(8)	Hacker [31]	HE	$H=\tan^{-1}\left(\frac{\frac{1}{2}(R-G)}{\frac{-1}{4}(R+G-2B)}\right)$
(9)	Wang *et al* [28]	Wang	$H=\frac{1}{2\pi}\left[\frac{\pi}{2}-\tan^{-1}\left(\frac{F}{\sqrt{3}}\right)+\theta\right]$ with $\theta=\begin{cases}0, & \text{if } G>B\\ \pi, & \text{if } G<B\end{cases}$

[a] $R'=255R,\ G'=255G,\ B'=255B$.
[b] $R''=R-min(R,G,B),\ G''=G-min(R,G,B),\ B''=B-min(R,G,B)$.
[c] $X=$ Brightness, intensity, lightness, or value.
[d] $(RGB)_{\mathrm{N}}^{\top}$ see [39].

Table B2. Available *RGB*-to-hue conversion algorithms[a,b,c,d] toward quantitative wall shear stress measurements, part (2/5).

Number	Citation	Algorithm (abbr.)	Hue
(10)	Kender [22]	Kender	$H=\begin{cases}\frac{\pi}{3}+\tan^{-1}\left(\frac{\sqrt{3}(G-R)}{(G-B)(R-B)}\right), & \text{if } R>B \text{ and } G\geqslant B\\ \pi+\tan^{-1}\left(\frac{\sqrt{3}(B-G)}{(B-R)(G-R)}\right), & \text{if } G>R\\ \frac{5\pi}{3}+\tan^{-1}\left(\frac{\sqrt{3}(R-B)}{(R-G)(B-G)}\right), & \text{else}\end{cases}$
(11)	Bajón *et al* [47]	Bajon	$H=\begin{cases}\frac{G-B}{3(R+G-2B)}, & \text{if } min(R,G,B)=B\\ \frac{B-R}{3(G+B-2R)}+\frac{1}{3}, & \text{if } min(R,G,B)=R\\ \frac{R-G}{3(R+B-2G)}+\frac{2}{3}, & \text{if } min(R,G,B)=G\end{cases}$
(12)	Kowalewski [34]	Kowalewski	$H=\begin{cases}63+\frac{63(G''-R'')}{G''+R''}, & \text{if } B''=0\\ 189+\frac{63(B''-G'')}{G''+B''}, & \text{if } R''=0\end{cases}$
(13)	Wiberg and Lior [32]	WL	$H=\begin{cases}\frac{1}{6}\left(\frac{G-B}{R''}\right)+1, & \text{if } R=max(R,G,B) \text{ and } G<B\\ \frac{1}{6}\left(\frac{G-B}{R''}\right), & \text{if } R=max(R,G,B) \text{ and } G>B\\ \frac{1}{6}\left(2+\frac{B-R}{G''}\right), & \text{if } G=max(R,G,B)\\ \frac{1}{6}\left(4+\frac{R-G}{B''}\right), & \text{if } B=max(R,G,B)\end{cases}$
(14)	Smith [10]	Smith	$H=\begin{cases}\theta, & \text{if } h\geqslant 0\\ 2\pi+\theta, & \text{else}\end{cases}$ with $\theta=\begin{cases}60(b-g), & \text{if } R=max(R,G,B)\\ 60(2+r-b), & \text{if } G=max(R,G,B)\\ 60(4+g-r), & \text{if } B=max(R,G,B)\end{cases}$

[a] $R'=255R,\ G'=255G,\ B'=255B$.
[b] $R''=R-min(R,G,B),\ G''=G-min(R,G,B),\ B''=B-min(R,G,B)$.
[c] $X=$ Brightness, intensity, lightness, or value.
[d] $(RGB)_{\mathrm{N}}^{\top}$ see [39].

Table B3. Available *RGB*-to-hue conversion algorithms[a,b,c,d] toward quantitative wall shear stress measurements, part (3/5).

Number	Citation	Saturation	X	Additional
(1)	Tenenbaum *et al* [20]	$S = 1 - \frac{min(R',G',B')}{I}$	$I = \frac{R'+G'+B'}{3}$	—
(2)	Tenenbaum *et al* [20]	$S = 1 - 3\,min(R,G,B)$	$I = \frac{R+G+B}{3}$	—
(3)	Kimura *et al* [27]	$S = \sqrt{sum\left[\left(r,g,b-\frac{1}{3}\right)^2\right]}$	$I = R_N + G_N + B_N$	$r = \frac{R}{I},\ g = \frac{G}{I},\ b = \frac{B}{I}$
(4)	Russ [37]	$S = 1 - \frac{min(R,G,B)}{I}$	$I = \frac{R+G+B}{3}$	—
(5)	Ohta *et al* [43]	$S = 1 - 3min(r,g,b)$	$I = \frac{R+G+B}{3}$	$r = \frac{R}{sum(R,G,B)},\ g = \frac{G}{sum(R,G,B)},\ b = \frac{B}{sum(R,G,B)}$
(6)	Matrox IM-1280 [29]	$S = \sqrt{2\left(V_1^2+V_2^2\right)}$	$I = \frac{R_N+G_N+B_N}{3}$	$\begin{pmatrix} I \\ V_1 \\ V_2 \end{pmatrix} = \begin{bmatrix} \frac{1}{3} & \frac{1}{3} & \frac{1}{3} \\ \frac{-1}{\sqrt{4}} & \frac{-1}{\sqrt{4}} & \frac{1}{\sqrt{2}} \\ \frac{1}{\sqrt{4}} & \frac{-1}{\sqrt{2}} & 0 \end{bmatrix} \begin{pmatrix} R \\ G \\ B \end{pmatrix}$
(7)	Pratt [36]	$S = \sqrt{V_1^2+V_2^2}$	$I = \frac{R_N+G_N+B_N}{3}$	$\begin{pmatrix} I \\ V_1 \\ V_2 \end{pmatrix} = \begin{bmatrix} \frac{1}{3} & \frac{1}{3} & \frac{1}{3} \\ \frac{-1}{\sqrt{6}} & \frac{-1}{\sqrt{6}} & \frac{2}{\sqrt{6}} \\ \frac{1}{\sqrt{6}} & \frac{-1}{\sqrt{6}} & 0 \end{bmatrix} \begin{pmatrix} R_N \\ G_N \\ B_N \end{pmatrix}$
(8)	Hacker [31]	—	—	—
(9)	Wang *et al* [28]	$S = 1 - \frac{min(R,G,B)}{I}$	$I = \frac{R+G+B}{3}$	$F = \begin{cases} R, & \text{if } G = B \\ \frac{2R-G-B}{G-B}, & \text{if } G \neq B \end{cases}$

[a] $R' = 255R,\ G' = 255G,\ B' = 255B$.
[b] $R'' = R - min(R,G,B),\ G'' = G - min(R,G,B),\ B'' = B - min(R,G,B)$.
[c] X = Brightness, intensity, lightness, or value.
[d] $(RGB)_N^{\top}$ see [39].

Table B4. Available *RGB*-to-hue conversion algorithms[a,b,c,d] toward quantitative wall shear stress measurements, part (4/5).

Number	Citation	Saturation	X	Additional
(10)	Kender [22]	$S = 1 - \frac{min(R,G,B)}{I}$	$I = \frac{R+G+B}{3}$	—
(11)	Bajón *et al* [25]	$S = 1 - \frac{min(R,G,B)}{I}$	$I = \frac{R+G+B}{3}$	—
(12)	Kowalewski [34]	$S = 1 - \frac{min(R'',G'',B'')}{I}$	$I = \frac{\sqrt{R^2+G^2+B^2}}{\sqrt{3}}$	—
(13)	Wiberg and Lior [32]	—	—	—
(14*)	Smith [10]	$S = \begin{cases} 1 - \frac{min(R,G,B)}{max(R,G,B)}, & \text{if } max(R,G,B) \neq 0 \\ 0, & \text{else} \end{cases}$	$V = max(R,G,B)$	$r = \frac{max(R,G,B)-R}{max(R,G,B)-min(R,G,B)}$ $g = \frac{max(R,G,B)-G}{max(R,G,B)-min(R,G,B)}$ $b = \frac{max(R,G,B)-B}{max(R,G,B)-min(R,G,B)}$
(14**)	Smith [10]	$S = \begin{cases} \frac{max(R,G,B)-min(R,G,B)}{max(R,G,B)+min(R,G,B)}, & \text{if } L \leqslant \frac{1}{2} \\ \frac{max(R,G,B)-min(R,G,B)}{2-max(R,G,B)-min(R,G,B)}, & \text{else} \end{cases}$	$L = \frac{max(R,G,B)+max(R,G,B)}{2}$	$r = \frac{max(R,G,B)-R}{max(R,G,B)-min(R,G,B)}$ $g = \frac{max(R,G,B)-G}{max(R,G,B)-min(R,G,B)}$ $b = \frac{max(R,G,B)-B}{max(R,G,B)-min(R,G,B)}$

[a] $R' = 255R,\ G' = 255G,\ B' = 255B$.
[b] $R'' = R - min(R,G,B),\ G'' = G - min(R,G,B),\ B'' = B - min(R,G,B)$.
[c] X = Brightness, intensity, lightness, or value.
[d] $(RGB)_N^{\top}$ see [39].

Table B5. Available *RGB*-to-hue conversion algorithms[a] toward quantitative wall shear stress measurements, part (5/5).

Number	Citation	Criterion				
		Equation (8)	Equation (9)	**(A)**	**(B)**	**(C)**
(1)	Tenenbaum *et al* [20]	○	●	●	●	●
(2)	Tenenbaum *et al* [20]	○	○	○	○	○
(3)	Kimura *et al* [27]	○	○	○	○	○
(4)	Russ [37]	○	●	○	○	○
(5)	Ohta *et al* [43]	●	●	○	○	○
(6)	Matrox IM-1280 [29]	●	○	○	○	○
(7)	Pratt [36]	●	●	○	○	○
(8)	Hacker [31]	●	●	○	○	○
(9)	Wang *et al* [28]	○	○	●	○	●
(10)	Kender [22]	○	●	●	●	●
(11)	Bajón *et al* [25]	●	●	●	●	●
(12)	Kowalewski [34]	●	○	●	●	●
(13)	Wiberg and Lior [32]	●	○	●	●	●
(14)	Smith [10]	○	●	●	○	●

[a] ● = met, ○ = not met.

ORCID iD

Stefanos Melekidis https://orcid.org/0000-0001-5063-5280

References

[1] Roach P E 1987 The generation of nearly isotropic turbulence by means of grids *Int. J. Heat Fluid Flow* **8** 82–92

[2] Reda D C and Muratore J J 1994 A new technique for the measurement of surface shear stress vectors using liquid crystal coatings *32nd Aerospace Sciences Meeting and Exhibit* (*Reno, Nevada, USA*) (Reston, VI: American Institute of Aeronautics and Astronautics) (https://doi.org/10.2514/6.1994-729)

[3] Fujisawa N, Funatani S and Kosaka S 2002 Measurement of shear-stress distribution by liquid-crystal coating *Proc. SPIE* **5058** 438

[4] Zhao J, Scholz P and Gu L 2011 Color change characteristics of two shear-sensitive liquid crystal mixtures (BCN/192, BN/R50C) and their application in surface shear stress measurements *Chin. Sci. Bull.* **56** 2897–905

[5] Demus D 1998 *Handbook of Liquid Crystals* (Weinheim: Wiley-VCH) (https://doi.org/10.1002/9783527619276)

[6] Stegemeyer H 1974 Helixstruktur und optische Aktivität in flüssigen Kristallen *Phys. Chem. Chem. Phys.* **78** 860–9

[7] Fergason J L 1966 Cholesteric structure-1 optical properties *Mol. Cryst.* **1** 293–307

[8] Reda D C, Wilder M C, Farina D J and Zilliac G 1997 New methodology for the measurement of surface shear stress vector distributions *J. Am. Inst. Aeronaut. Astronaut.* **35** 608–14

[9] Rösgen T and Totaro R 2002 A statistical calibration technique for thermochromic liquid crystals *Exp. Fluids* **33** 732–4

[10] Smith A R 1978 Color gamut transform pairs *ACM SIGGRAPH Comput. Graph.* **12** 12–19

[11] Bonnett P 1989 Application of liquid crystals in aerodynamic testing *PhD Thesis* University of Oxford

[12] Wilder M C 1998 Uncertainty analysis of the liquid crystal coating shear vector measurement technique *20th AIAA Advanced Measurement and Ground Testing Technology Conf.* (*Albuquerque, New Mexico, USA*) (Reston, VI: American Institute of Aeronautics and Astronautics) p 95

[13] Zhao J 2019 Investigation on wall shear stress measurement in supersonic flows with shock waves using shear-sensitive liquid crystal coating *Aerosp. Sci. Technol.* **85** 453–63

[14] Melekidis S, Elfner M R and Bauer H-J 2020 Towards quantitative wall shear stress measurements: calibration of liquid crystals *Proc. ASME Turbo Expo 2020: Turbomachinery Technical Conf. and Exposition* (Controls, Diagnostics, and Instrumentation; Cycle Innovations; Cycle Innovations: Energy Storage vol 5) (*Virtual, Online, 21–25 September 2020*) (https://doi.org/10.1115/GT2020-14381)

[15] Preston J H 1954 The determination of turbulent skin friction by means of pitot tubes *Aeronaut. J.* **58** 109–21

[16] Ellis S R and Gay B 1959 The parallel flow of two fluid streams: interfacial shear and fluid-fluid interaction *Trans. Instn. Chem. Eng.* **37** 206–13

[17] Schlichting H, Gersten K and Krause E 2006 *Grenzschicht-Theorie: Mit 22 Tabellen* 10th edn (Berlin: Springer) (https://doi.org/10.1007/3-540-32985-4)

[18] Plesniak M and Peterson S 2004 Wall shear stress measurements for conventional applications and biomedical flows *24th AIAA Aerodynamic Measurement Technology and Ground Testing Conf. (Portland, OR, 28 June 2004–1 July 2004)* (Reston, VI: American Institute of Aeronautics and Astronautics) (https://doi.org/10.2514/6.2004-2301)

[19] Schneider M 1995 Untersuchungen zum lokalen konvektiven Wärmeübergang in Gasturbinen: axiale Schaufelgitter mit *Radialspalt Dissertation* Universität Karlsruhe and Arizona State University, Institut für Thermische Strömungsmaschinen and Department of Mechanical and Aerospace Engineering

[20] Tenenbaum J M, Garvey T D, Weyl S and Wolf H C 1974 *An Interactive Facility for Scene Analysis Research* Technical Note 95 (Artificial Intelligence Center)

[21] Ireland P T and Jones T V 2000 Liquid crystal measurements of heat transfer and surface shear stress *Meas. Sci. Technol.* **11** 969–86

[22] Kender J R 1976 *Saturation, Hue, And Normalized Color: Calculation, Digitization Effects, and Use* Technical Note 77 (Pittsburgh, PA: Carnegie-Mellon University, Department Of Computer Science)

[23] Palus H and Bereska D 1995 The comparison between transformations from RGB colour space to IHS colour space, used for object recognition *5th Int. Conf. on Image Processing and its Applications* (IEEE) pp 825–7

[24] Foley J D, van Dam A and Feiner S K 1995 *Computer Graphics: Principles and Practice* 2nd edn (Reading, MA: Addison-Wesley Publishing Company)
[25] Bajón J, Cattoen M and Kim S D 1985 Techniques de transformations colorimetriques en temps reel implantees sur un module de vision pour la robotique *Actes Conf. MICAD* 76–86
[26] Dabiri D 2009 Digital particle image thermometry/velocimetry: a review *Exp. Fluids* **46** 191–241
[27] Kimura I, Takamori T, Yamauchi H, Ozawa M, Takenaka N and Sakaguchi T 1988 Simultaneous measurement of flow and temperature fields based on color image information *Nagare No Kashika* **8** 185–8
[28] Wang Z, Ireland P T, Jones T V and Davenport R 1994 A colour image processing system for transient liquid crystal heat transfer experiments *J. Turbomach.* **118** 421–7
[29] Farina D J, Hacker J M, Moffat R J and Eaton J K 1994 Illuminant invariant calibration of thermochromic liquid crystals *Exp. Therm. Fluid Sci.* **9** 1–12
[30] Hay J L and Hollingsworth D K 1996 A comparison of trichromic systems for use in the calibration of polymer-dispersed thermochromic liquid crystals *Exp. Therm. Fluid Sci.* **12** 1–12
[31] Hacker J M 1995 Heat transfer measurements in a backward facing step flow with arbitrary wall temperature variations *PhD Thesis* Stanford University
[32] Wiberg R and Lior N 2004 Errors in thermochromic liquid crystal thermometry *Rev. Sci. Instrum.* **75** 2985–94
[33] Kowalewski T A 1999 Particle image velocimetry and thermometry using thermochromic liquid crystals *Int. Symp. on Particle Image Velocimetry* (*Göttingen, Germany, 17–19 September 2001*)
[34] Kowalewski T A, Ligrani P, Dreizler A, Schulz C and Fey U 2007 Temperature and Heat Flux *Handbook of Experimental Fluid Mechanics* (Berlin: Springer) pp 487–561
[35] Kodzwa P M and Eaton J K 2007 Angular effects on thermochromic liquid crystal thermography *Exp. Fluids* **43** 929–37
[36] Pratt W K 2013 *Introduction to Digital Image Processing* (Hoboken, NJ: CRC Press)
[37] Russ J C 2011 *The Image Processing Handbook* 6th edn (Boca Raton, FL: CRC Press)
[38] Dabiri D and Gharib M 1991 Digital particle image thermometry: the method and implementation *Exp. Fluids* **11** 77–86
[39] Pratt W K 1991 *Digital Image Processing* (*A Wiley-Interscience Publication*) 2nd edn (New York: Wiley)
[40] Ziemba A and Fornalik-Wajs E 2014 Transformation of colour space dedicated to an experimental analysis fulfilling the applicability criteria *J. Phys.: Conf. Ser.* **530**
[41] Ziemba A and Fornalik-Wajs E 2016 Evaluation of colour space transformation suitability to optical temperature measurements *J. Phys.: Conf. Ser.* **745** 032108
[42] Ziemba A and Fornalik-Wajs E 2018 Time performance of RGB to HSI colour space transformation methods *Arch. Thermodyn.* **39** 111–28
[43] Ohta Y-I, Kanade T and Sakai T 1980 Color information for region segmentation *Comput. Graph. Image Process.* **13** 222–41
[44] Park H G, Dabiri D and Gharib M 2001 Digital particle image velocimetry/thermometry and application to the wake of a heated circular cylinder *Exp. Fluids* **30** 327–38
[45] Tollmien W, Schlichting H, Görtler H and Riegels F W 1904 Über Flüssigkeitsbewegung bei sehr kleiner Reibung *Verhandl. III, Internat. Math.-Kong., (Heidelberg, 1904)* pp 575–84
[46] LCRHallcrest 2014 *Handbook of Thermochromic Liquid Crystal Technology* (available at: https://cupdf.com/document/lcr-hallcrest-handbook-of-liquid-crystal-technology-rt006-rev01- usa.html?page=2) (Accessed16 February 2022)
[47] Bajón J, Cattoen M and Liang L 1986 Identification of multicoloured objects using a vision module *Proc. 6th Int. Conf. on Robot Vision and Sensory Controls (RoViSeC)* (*Paris, France, 3–5 June 1986*) pp 21–30